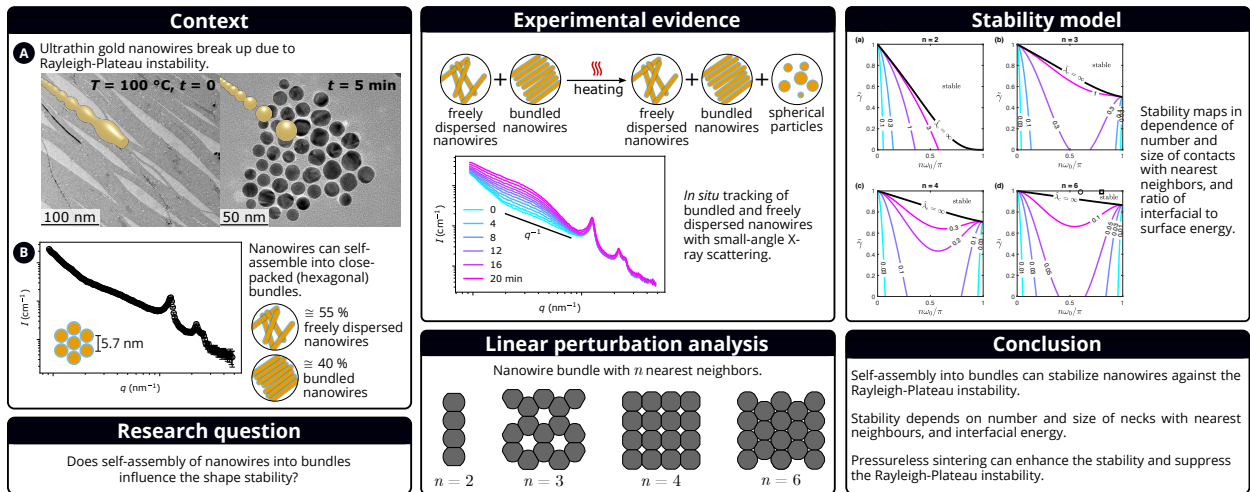# Graphical Abstract

Stabilization of ultrathin nanowires by self-assembly into bundles

Simon Bettscheider, Tobias Kraus, Norman A. Fleck

Context

A Ultrathin gold nanowires break up due to Rayleigh-Plateau instability.

$T = 100\ °C,\ t = 0$ $t = 5\ min$

100 nm   50 nm

B

I (cm^{-1})

q (nm^{-1})

5.7 nm

Nanowires can self-assemble into close-packed (hexagonal) bundles.

$\cong$ 55 % freely dispersed nanowires

$\cong$ 40 % bundled nanowires

Research question

Does self-assembly of nanowires into bundles influence the shape stability?

Experimental evidence

freely dispersed nanowires + bundled nanowires → heating → freely dispersed nanowires + bundled nanowires + spherical particles

I (cm^{-1})

0
4
8
12
16
20 min

q^{-1}

q (nm^{-1})

In situ tracking of bundled and freely dispersed nanowires with small-angle X-ray scattering.

Linear perturbation analysis

Nanowire bundle with n nearest neighbors.

$n = 2$ $n = 3$ $n = 4$ $n = 6$

Stability model

(a) $n = 2$
(b) $n = 3$
(c) $n = 4$
(d) $n = 6$

$\bar{\gamma}$

$n\omega_0/\pi$

Stability maps in dependence of number and size of contacts with nearest neighbors, and ratio of interfacial to surface energy.

Conclusion

Self-assembly into bundles can stabilize nanowires against the Rayleigh-Plateau instability.

Stability depends on number and size of necks with nearest neighbours, and interfacial energy.

Pressureless sintering can enhance the stability and suppress the Rayleigh-Plateau instability.

Stabilization of ultrathin nanowires
by self-assembly into bundles

Simon Bettscheider[a,b], Tobias Kraus[a,b,*], Norman A. Fleck[c,*]

[a]*INM – Leibniz Institute for New Materials, Campus
D2.2, Saarbrücken, 66123, Germany*
[b]*Colloid and Interface Chemistry, Saarland University, Campus
D2.2, Saarbrücken, 66123, Germany*
[c]*Cambridge University Engineering Department, Trumpington Street, Cambridge, CB2
1PZ, UK*

Abstract

The relative tendency of freely dispersed and bundled gold nanowires to break up along their length by the Rayleigh-Plateau instability is investigated both experimentally and theoretically. Small angle X-ray scattering, in combination with transmission electron microscopy, reveal that the bundling of nanowires can enhance their stability. Theoretical support for this observation is provided by a linear perturbation analysis of a representative unit cell of bundled wires. A stability map is constructed for a bundle of nanowires to display the sensitivity of the Rayleigh-Plateau instability to the number and size of contacts with nearest neighbors per nanowire, and to the ratio of interfacial energy to surface energy. Stabilisation is enhanced by allowing the bundle of wires to sinter freely: a criterion for this kinetically-based stabilisation is given in terms of the ratio of pinch-off time for the instability to

---

*Authors to whom correspondence should be addressed.
Email addresses: `simon.bettscheider@leibniz-inm.de` (Simon Bettscheider),
`tobias.kraus@leibniz-inm.de` (Tobias Kraus), `naf1@eng.cam.ac.uk` (Norman A.
Fleck)

the sintering time to form the necks between nanowires.

---

1. Introduction

Ultrathin nanowires of length to diameter aspect ratio exceeding 10^3 are now readily available. They are prepared by chemically reducing a metal or semiconductor salt in the presence of an organic ligand [1]. The ligand directs one-dimensional growth of the nanowire by binding to the nanowire surface; additionally, the ligand stabilizes the nanowire core and the colloidal dispersion [2, 3, 4, 5, 6]. To date, ultrathin nanowires have been made from metals and their alloys (gold [7, 8, 9, 10, 3], iron-platinum [11], silver [12], ruthenium [13]) and semiconductors (copper sulfide [14], bismuth sulfide [15], antimony sulfide [16]). The nanowires are flexible and can spontaneously form continuous 2D and 3D superstructures; this tendency has been exploited to assemble opto-electronic devices [17, 18, 19]. Ultrathin nanowires have also been used in stretchable and optically transparent supercapacitors [17], in electrocatalytic membranes [20], and in the printed electrodes of bendable touchscreens [18].

A fundamental challenge for nanowire manufacture and use is their stability. Cylindrical wires are thermodynamically unfavorable in shape: a circular cylinder has a greater surface area, and consequently greater interfacial energy, than an array of spheres of the same overall volume, provided the ratio of the radius of spheres to that of the cylinder exceeds $(3\pi/2)^{\frac{1}{3}}$ [21, 22]. This difference in surface energy drives the so-called Rayleigh-Plateau instabil-

ity [23, 24], also known as the morphological, geometric, shape, or Rayleigh instability. The evolution in shape of a circular cylindrical wire into spherical droplets by surface diffusion has been analyzed by Nichols and Mullins [21, 22]; the bulk of the wire is taken to be rigid and diffusional flow occurs in the axial direction along the surface of the wire. The time required for break-up is proportional to the fourth power of the cylinder radius so that thin wires are particularly prone to degradation [21, 22]. In practice, ultrathin gold nanowires in a dispersion fragment over a few weeks at room temperature, and over a few minutes at 100 °C.

Both energetic and kinetic considerations play a role in stabilizing nanowires against the Rayleigh-Plateau instability [25]. Stabilization by energetic contributions can be enhanced by the presence of a substrate [26, 27, 28, 29], by anisotropy of the nanowire's surface energy [30, 31, 32, 33], and by geometrical confinement in a matrix [34, 35, 36]. The addition of a ligand shell can enhance stability both energetically and kinetically [25]. For example, the ligand shell can reduce the nanowire's surface energy and slow down diffusion [25, 37, 38, 34, 39, 40].

Surprisingly little is known about the stabilization of nanowires by their self-assembly into a bundle. Commonly, ultrathin nanowires are synthesized as colloids, and the resulting dispersion can comprise individual wires or wires that have self-assembled into close-packed bundles [1, 19, 41]. The size and relative density (also called packing density) of the bundles depend upon the choice of solvent [41], ligand type [40], and ligand shell density [42]. For example, the bundling of ultrathin gold nanowires (AuNWs) can be driven by a phase separation between the ligand shell and the solvent,

or by depletion forces induced by the solvent or unbound ligand molecules [43, 42]. Bundles also form when the nanowire dispersions are dried [44, 18]. The center-to-center spacing of the wires ranges from 4.1 nm [43] to 5.9 nm [42], depending upon the method of self-assembly.

In the following, we show that the formation of bundles affects the shape stability of nanowires. The break-up of both fully dispersed and bundled nanowires is observed *in situ* by small-angle X-ray scattering. An analytical model is introduced to predict the influence of bundling upon shape stability. Stability maps are generated using a linear perturbation analysis, and are compared with the experimental results of the present study and with those reported in the literature.

2. Experimental methods

2.1. Synthesis of ultrathin gold nanowires

Chemicals and materials. All chemicals used are listed in Table S1 in the supplementary information.

Synthesis. Ultrathin gold nanowires (AuNWs) were synthesized using a protocol based upon that of Feng et al. [45] and Nouh et al. [40]. In a typical synthesis, 60 mg of the dry precursor $HAuCl_4 \cdot nH_2O$ was placed in a glass vial and quickly covered with a volume of 9.9 mL of n-hexane; 2.04 mL of the ligand oleylamine was added while flushing with Ar. The mixture was vortexed for 5 min to dissolve the precursor. Finally, 3.06 mL of the reducing agent triisopropylsilane was added while flushing with Ar. The mixture was again vortexed for 30 s and the solution was rested, without stirring, at 25 °C for 24 h.

5

Purification. The reaction product was purified twice by adding two volumes of ethanol (30 mL each), centrifugating at 100 rcf for 1 min to precipitate the AuNWs, and redispersing in *n*-hexane after the first purification cycle and cyclooctane after the second purification cycle.

2.2. Heating of nanowires and in situ small-angle X-ray scattering

The break-up of nanowires was monitored *in situ* by small-angle X-ray scattering (SAXS). Samples for observation in SAXS were kept at room temperature for at least 16 h after purification before transferring them into glass capillaries with an inner diameter of 1.5 mm. To accelerate the break-up, the samples were heated *in situ* to either 60 °C or 70 °C. The heating stage was pre-heated to the desired temperature, and measurements were taken at 2 min intervals in the beamline of a Cu Kα X-ray source (SAXS setup XEUSS 2.0, XENOCS, France). The scattered intensity was captured by a detector at a distance of approximately 1.2 m from the sample. The sample-to-detector distance was calibrated with a standard of silver behenate prior to each measurement. The two-dimensional scattering images were integrated (azimuthal integration) using the software Foxtrott (Synchrotron Soleil, France) to obtain scattering curves.

The (center-to-center) interwire distance d inside bundles of AuNWs was determined assuming Bragg scattering [46] using the formula

$$d = \frac{4\pi}{\sqrt{3}q_{uv}}\sqrt{u^2 + uv + v^2} \tag{1}$$

where q_{uv} is the value of the q-vector of the Bragg scattering peak of a two-dimensional hexagonal lattice of Miller indices u and v [46].

2.3. Scattering model fits

The volume fractions of gold in the form of bundled nanowires, freely dispersed nanowires, and spherical particles in the dispersion were obtained by fitting a scattering model to the SAXS data. The model was based on the work of Sundblom et al. [47], Manet et al. [48], and Loubat et al. [19] and used the form factors of cylinders and spheres and the structure factor of crystalline cylinders. Freely dispersed nanowires were modeled using the form factor of a cylinder convoluted with a Schulz-Zimm distribution to account for the distribution of their diameters. Bundles of nanowires were modeled by multiplying this form factor with the structure factor of a 2D hexagonal lattice. The structure factor was approximated by a sum of Lorentzian functions at the positions of the Bragg peaks. A Debye-Waller factor accounted for disorder in the 2D hexagonal lattice, for example caused by thermal fluctuations. Spherical nanoparticles were modeled by convoluting the form factor of spheres with a Schulz-Zimm distribution. All spherical particles (formed during the synthesis and during break-up) were consolidated in a single, broadly distributed function whose mean diameter was allowed to evolve with time. The overall scattered intensity was the volume-weighted sum of the scattered intensity of freely dispersed nanowires, bundled nanowires, and spherical nanoparticles. Details on the model can be found in the supplementary information. The fits were implemented in Python using the library LMFIT [49].

2.4. Transmission electron microscopy

Small aliquots of the heated samples were prepared for *ex situ* observation by transmission electron microscopy. To this end, the aliquots were diluted to a

concentration of approximately [Au] = 0.05 mg/mL and 5 µL of the diluted sample was drop cast on a perforated carbon-coated grid (Plano, Germany). The perforated grid reduced drying artefacts when compared to standard carbon-coated grids. The samples were observed at an acceleration voltage of 200 kV in a JEM 2010 (JEOL, Japan) transmission electron microscope (TEM).

3. Experimental results

3.1. Ex situ transmission electron micrographs

Ultrathin gold nanowires (AuNWs) were chemically synthesized using the protocol detailed above, dried on carbon-coated grids, and analyzed in a Transmission Electron Microscope (TEM). A typical micrograph (Fig. 1a,b) shows nanowires with uniform gold cores and diameters of 1.6 nm and a spacing of 4.4 nm that is caused by a monolayer of the ligand oleylamine on the metal. The length of the nanowires exceeded the field of view and was estimated to be above 1 µm; lengths of 1 to 4 µm have been reported previously [50].

Heating of the AuNW dispersions to 60 °C resulted in fragmentation of the nanowires. Samples that were kept at 60 °C for 10 min contained an increased fraction of spheres (Fig. 1c,d) that further grew after 20 min at 60 °C, whereupon much of the micrograph was covered with spherical particles (Fig. 1e,f).

The fragmentation of gold nanowires has been explained in terms of the Rayleigh-Plateau instability [39, 25]. Here, we are interested in the relative stability of bundled and freely dispersed wires. We used X-ray scattering

8

to quantify the volume fractions of intact and fragmented wires at elevated temperatures.

3.2. In situ small-angle X-ray scattering

Small-angle X-ray scattering (SAXS) from the AuNWs in cyclooctane at $20\,°C$ is shown in Fig. 2b. The scattered intensity depends on the shape of the particles ("form factor") and their relative arrangement ("structure factor") [46]. A dispersion of free AuNW has its scattering determined only by the form factor, as reported in [41, 42], for example.

Scattering from the samples used here (Fig. 2b) was dominated by the form factor for scattering vectors $q < 1\,\mathrm{nm}^{-1}$, while the structure factor dominated for $q > 1\,\mathrm{nm}^{-1}$. Hexagonally packed AuNW bundles caused distinct peaks in the scattered intensity at $1.27\,\mathrm{nm}^{-1}$, $2.20\,\mathrm{nm}^{-1}$, and $2.52\,\mathrm{nm}^{-1}$. Such bundles have been reported previously [45, 19, 41]. They are caused by attractive, entropic interactions that are due to unbound ligands and linear solvent molecules that align between the wires [43, 42]. The peak positions indicate a center-to-center spacing of the wires of $d = 5.7\,\mathrm{nm}$. Scattering models (discussed in the next section) revealed that the dispersion contained a fraction of approximately $55\,\%$ in dispersed nanowires and $40\,\%$ in nanowire bundles.

The fragmentation of wires through the Rayleigh-Plateau instability was initiated by heating the dispersion of wires and bundles to $60\,°C$ and tracked via SAXS. Scattering measurements at $2\,\mathrm{min}$ intervals are shown in Fig. 2c. The scattered intensity initially scaled with q^{-1} in the region dominated by the form factor ($q < 1\mathrm{nm}^{-1}$), which is typical for cylindrical objects. The overall scattering in this region gradually increased, indicating the formation

9

of spherical particles. The overall scattering in the region dominated by the structure factor ($q > 1 \text{nm}^{-1}$) remained unchanged, indicating that the bundles did not fragment.

3.3. Interpretation of scattering data

The scattering model described in section 2.3 was used to extract quantitative volume fractions of the gold contained in dispersed nanowires, bundled nanowires, and spherical particles from the time-dependent SAXS (Fig. 2d,e). The original gold volume fractions were $54.8 \pm 1.8\,\%$ in freely dispersed nanowires, $40.4 \pm 1.2\,\%$ in bundled nanowires, and $4.7 \pm 0.5\,\%$ in spherical nanoparticles. The fraction of gold in freely dispersed nanowires decreased linearly to $39.0 \pm 1.3\,\%$ over $20\,\text{min}$ at $60\,^{\circ}\text{C}$, while that of spherical particles increased to $21.2 \pm 0.3\,\%$. This corresponds to a fragmentation rate of approximately $6.5\,\text{km s}^{-1}\,\text{mL}^{-1}$ of freely dispersed nanowires.

The volume fraction of bundled nanowires remained constant (Fig. 2e). Heating to $70\,^{\circ}\text{C}$ led to the same qualitative results (Fig. S1 in the supplementary information): freely dispersed nanowires broke up and bundled nanowires remained mainly intact. Note that an elevated temperature can induce the formation of bundles, too [42]. The formation and dissociation of bundles occurs over a time scales of hours [41], and is hence independent of the break-up that is observed over minutes.

The results of SAXS and TEM analysis, taken together, indicated the rapid fragmentation of dispersed AuNWs, but not of AuNWs in bundle form. We conclude that AuNWs stabilize each other in bundles. The following sections provide an analytical model for the stability of nanowires in bundles to provide additional insights into this observation.

4. Analytical model for Rayleigh-Plateau instability of a bundle of nanowires

The prototypical problem is sketched in Fig. 3, showing the progressive break-down of a cylindrical wire into discrete droplets. The wire resides in a vertical stack of fixed height and so the necks between neighboring wires can be idealized by fixed planes.

4.1. Geometry

A representative nanowire within a bundle is modeled as a circular cylinder of radius R truncated by $n \geq 2$ flat surfaces, each representing the neck with a neighboring wire, as shown in Fig. 4. Values of n for tessellation are $n = 2, 3, 4, 6$.

Our aim is to explore the possibility of diffusional flow of atoms along the surface of the wire in the axial direction in order to perturb the shape from prismatic to one where the cross-section varies with the axial coordinate z. Assume that the radius $R(z, t)$ evolves with time t and varies harmonically with axial position z. Suppose that the radius of the cylinder is perturbed from the uniform reference state $R = R_0$ to the state

$$R(z, t) = R_0 + \Delta R(t) + a(t) \cos{(kz)}, \tag{2}$$

where $a(t)$ is the perturbation amplitude, λ is the perturbation wavelength, and $k = 2\pi/\lambda$ is the corresponding wavenumber (Fig. 5b). The term $\Delta R(t)$ results from the constraint that the cylinder maintains a constant overall mass. The shape (2) has the following interpretation. In general, assume that an initial imperfection exists at $t_I = 0$, and is of amplitude $a(t_I = 0) > 0$

11

and wavelength λ. Our aim is to seek an expression for the rate of growth of the imperfection $\dot{a}(t)$.

The evolution in shape of the wire occurs at fixed value of relative density of the bundle of wires. Thus, the center-to-center spacing of adjacent wires $2H$ is held constant, and the contact angle $\omega(z, t)$ evolves with $R(z, t)$ such that

$$\cos \omega = \frac{H}{R}. \tag{3}$$

In the unperturbed reference state, $R = R_0$, the contact angle equals ω_0, where $\cos \omega_0 = H/R_0$. Note that ω is *not* the local contact angle as dictated by local equilibrium of surface energies for the wire. Rather, ω is a macroscopic measure of the wire inclination at the edge of the contact. This approximation has been justified by Parhami et al. [51] for the sintering of a row of spherical particles. Example configurations for a bundle of wires are shown in Fig. S2, and the relative density as a function of ω_0 is given in Fig. S3 for the unperturbed state, $a = 0$. The perturbation analysis of the present study builds upon that of Gill [28]; he considered the case of a single wire on a surface, for which H is free to evolve with time.

4.2. Conservation of cylinder mass

The term $\Delta R(t)$ in (2) is determined from conservation of volume over the wavelength λ as follows. The cross-section of the wire A_z^0 in the unperturbed state is

$$A_z^0 = \pi f_0 R_0^2, \tag{4}$$

12

where

$$f_0 \equiv 1 - \frac{n}{\pi} \left(\omega_0 - \frac{1}{2} \sin\left(2\omega_0\right) \right). \tag{5}$$

Consequently, the volume V_0 of a length λ of the wire in the unperturbed state is $V_0 = A_z^0 \lambda$. Now consider the perturbed state. The cross-sectional area A_z of the cylinder at any axial position z is

$$A_z(z, t) = \pi f R^2, \tag{6}$$

where

$$f(\omega, n) \equiv 1 - \frac{n}{\pi} \left(\omega - \frac{1}{2} \sin\left(2\omega\right) \right). \tag{7}$$

Now write $\omega(z) = \omega_0 + \Delta\omega(z)$ to give, via (3),

$$\Delta\omega = \left(\frac{\Delta R}{R_0} + \frac{a}{R_0} \cos\left(kz\right) - \frac{a^2}{R_0^2} \cos^2\left(kz\right) \right) \cot\omega_0 + \mathcal{O}(a^3). \tag{8}$$

We use (8) to re-write $f(\omega, n)$ as

$$f(\omega, n) = f_0 - \frac{n}{\pi} \left(\Delta\omega(1 - \cos\left(2\omega_0\right)) + \Delta\omega^2 \sin\left(2\omega_0\right) \right). \tag{9}$$

Introduce the compact notation

$$\xi_1(\omega_0, n) \equiv \pi - n \left(\omega_0 - \frac{1}{2} \sin\left(2\omega_0\right) \right) = \pi f_0 \tag{10}$$

$$\xi_2(\omega_0) \equiv 1 - \cos\left(2\omega_0\right), \tag{11}$$

13

to write the current cross-sectional area $A_z(z,t)$ as

$$A_z = \pi R_0^2 \left(f_0 + \frac{\Delta\omega}{\pi} \left(2\xi_1 \tan\omega_0 - n\xi_2 \right) \right. \tag{12}$$
$$\left. + \frac{\Delta\omega^2}{\pi} \left(3\xi_1 \tan^2\omega_0 - 2n\xi_2 \tan\omega_0 - n\sin(2\omega_0) \right) \right).$$

Conservation of volume dictates that the current volume of the cylinder over one wavelength, $V = \int_0^\lambda A_z \, dz$, equals the volume $V_0 = \pi R_0^2 f_0 \lambda$ in the unperturbed state, and consequently

$$\frac{\Delta R}{R_0} = \xi_3(\omega_0) \left(\frac{a}{R_0} \right)^2, \tag{13}$$

where

$$\xi_3(\omega_0, n) \equiv \frac{-\xi_1 + n\xi_2 \cot\omega_0 + n\sin(2\omega_0) \cot^2\omega_0}{4\xi_1 - 2n\xi_2 \cot\omega_0}. \tag{14}$$

Note that ΔR is $\mathcal{O}(a^2)$.

4.3. Energetics: surface energy as driving force

The driving force for the Rayleigh-Plateau instability is the reduction in total surface energy that accompanies growth of the perturbation. The interface between neighboring wires possesses an interfacial free energy per unit area γ_c, and the free surface of the wire has a surface energy per unit area γ_s.

In the present study, the ligand shell is not considered separately. Effects of the ligand shell can be incorporated by modifying the effective values of surface energies and diffusivities. Effective values could be obtained from advanced quantum chemical simulations [52]. Our earlier work showed how

14

such atomistic and molecular information can be incorporated into the effective surface energy and diffusivity values [25].

4.4. Kinematics: shape evolution by surface diffusion

The shape of each nanowire evolves by surface diffusion in the axial direction [21, 22]. Conservation of mass requires that the surface divergence of the surface diffusive flux $\boldsymbol{j}$ and the normal velocity of matter deposited onto the surface v_n sum to zero,

$$\boldsymbol{\nabla}_{\mathrm{s}} \cdot \boldsymbol{j} + v_n = 0, \tag{15}$$

where $\boldsymbol{\nabla}_{\mathrm{s}}$ is the usual surface divergence operator, and a bold symbol denotes a vector throughout this paper. Assume that the dominant surface flux is in the axial direction and is of magnitude j. Then, (15) simplifies to

$$\frac{1}{R}\frac{\partial(Rj)}{\partial s} + v_n = 0, \tag{16}$$

where s is the arc length along the free surface (see Fig. 5b). The normal velocity of matter deposited on the surface must equal the rate of change in radius, $v_n = \dot{R} = \dot{a}\cos(kz) + \mathcal{O}(a^2)$. For small perturbations ($a \ll R$), we may write $R^{-1}\partial(Rj)/\partial s \approx \partial j/\partial z$ for the derivative in (16). Consequently, the surface flux j is

$$j = -\frac{\dot{a}}{k}\sin(kz) + \mathcal{O}(a^2). \tag{17}$$

15

5. Linearised perturbation analysis

5.1. Stability map and critical wavenumber

The presence of a perturbation changes the Gibb's free energy of the wire
over one wavelength λ by ΔG, where

$$\Delta G = \gamma_{\mathrm{s}}(A_{\mathrm{s}} - A_{\mathrm{s}}^0) + \gamma_{\mathrm{c}}(A_{\mathrm{c}} - A_{\mathrm{c}}^0). \tag{18}$$

Here, A_{s} is the area of the free surface and A_{c} is the area at the constraining
neck over one wavelength, as shown in Fig. 5a. The superscript 0 denotes
the respective area in the unperturbed state.

The free surface area of the wire over one wavelength λ of the perturbation
is

$$A_{\mathrm{s}} = \int_0^\lambda 2(\pi - n\omega)R \; \mathrm{d}s. \tag{19}$$

For small perturbations, we can write

$$\mathrm{d}s = \left(1 + \frac{1}{2}(ak)^2 \sin^2(kz) + \mathcal{O}(a^4)\right) \mathrm{d}z. \tag{20}$$

Now make use of (8) to obtain

$$A_{\mathrm{s}} = A_{\mathrm{s}}^0 \left(1 + \left(\xi_3\xi_4 + \frac{1}{4}(R_0 k)^2\right)\frac{a^2}{R_0^2}\right), \tag{21}$$

where ξ_4 is defined by

$$\xi_4(\omega_0, n) \equiv \frac{\pi - n\omega_0 - n\cot\omega_0}{\pi - n\omega_0} \tag{22}$$

and $A_{\mathrm{s}}^0 = 2(\pi - n\omega_0)R_0\lambda$ is the surface area of the free surface of the unperturbed cylinder. Note from (21) that $(A_{\mathrm{s}} - A_{\mathrm{s}}^0)$ is second-order in a/R_0.

The contact area A_{c} over one wavelength is

$$A_{\mathrm{c}} = 2n \int_0^\lambda R \sin\omega \; \mathrm{d}z, \tag{23}$$

and can be re-written in terms of a/R_0 by making use of the expression

$$\frac{\sin\omega}{\sin\omega_0} = 1 + \Delta\omega \cot\omega_0 - \frac{1}{2}\Delta\omega^2 + \mathcal{O}(\Delta\omega^3), \tag{24}$$

and by expressing the radius R in terms of $\Delta\omega$ via (3), such that

$$\frac{R}{R_0} = 1 + \Delta\omega \tan\omega_0 + \Delta\omega^2 \tan^2\omega_0. \tag{25}$$

Now make use of (8), along with (24) and (25) to express (23) as

$$A_{\mathrm{c}} = A_{\mathrm{c}}^0 \left(1 + \xi_5 \frac{a^2}{R_0^2}\right), \tag{26}$$

where

$$\xi_5(\omega_0, n) \equiv \xi_3 + \xi_3 \cot^2\omega_0 - \frac{1}{4}\cot^2\omega_0 \tag{27}$$

and $A_{\mathrm{c}}^0 = 2nR_0\lambda \sin\omega_0$ is the contact area in the unperturbed, reference state over one wavelength. The result for A_{c} is also second-order in a/R_0.

Substitute the expressions (21) and (26) into the definition of Gibb's free energy change (18), and introduce the ratio of interfacial free energies

$\tilde{\gamma} = \gamma_{\mathrm{c}}/\gamma_{\mathrm{s}}$, to obtain

$$\Delta G = \gamma_{\mathrm{s}} A_{\mathrm{s}}^0 \left(\frac{a}{R_0}\right)^2 \left(\xi_3 \xi_4 + \frac{1}{4}(R_0 k)^2 + \frac{\tilde{\gamma} \xi_5 n \sin \omega_0}{\pi - n\omega_0}\right). \tag{28}$$

The nanowire is stable against the formation of a perturbation of amplitude a and wavelength λ if $\Delta G \geq 0$. This is satisfied for wavelengths $\lambda \leq \lambda_{\mathrm{c}}$, where the critical perturbation wavelength λ_{c} for which $\Delta G = 0$ is given in non-dimensional form by

$$\tilde{\lambda} \equiv \frac{\lambda_{\mathrm{c}}}{2\pi R_0} = \frac{1}{2}\left(-\xi_3 \xi_4 - \frac{\tilde{\gamma} \xi_5 n \sin \omega_0}{\pi - n\omega_0}\right)^{-\frac{1}{2}}. \tag{29}$$

We note in passing that $\xi_3 > 0$, $\xi_4 < 0$, and $\xi_5 > 0$ and consequently $\tilde{\lambda}$ is real in (29). The wavenumber corresponding to λ_{c} is $k_{\mathrm{c}} = 2\pi/\lambda_{\mathrm{c}}$, and for later use, we emphasize that the tilde over the symbol λ denotes the non-dimensional quantity $\tilde{\lambda} \equiv \lambda/(2\pi R_0)$. The stability maps in Fig. 6 illustrate (29) in graphical form, and show the sensitivity of $\tilde{\lambda}_{\mathrm{c}}$ to n, $\tilde{\gamma}$, and ω_0. It is evident from Fig. 6 that a region ($\tilde{\lambda}_{\mathrm{c}} = \infty$) exists in the top-right of each map for which the bundle is stable against break-up into discrete droplets. Stability is enhanced by a large value of $\tilde{\gamma}$, a large value of ω_0 (corresponding to a high relative density of the bundle), and by a small co-ordination number n. For reference, a free standing circular cylindrical wire is unstable for all wavelengths exceeding $\lambda_{\mathrm{c}} = 2\pi R_0$, as discussed by Nichols and Mullins [21, 22]: thus, $\tilde{\lambda}_{\mathrm{c}}$ equals unity for the free standing wire.

5.2. Perturbation growth rate and fastest growing perturbation

313 We proceed to use the Cocks-Suo variational principle [53, 51, 28] to de-

314 rive the wavenumber of the fastest growing perturbation. The variational

315 functional is defined as $\Pi(\dot{a}) = \Delta\dot{G}(\dot{a}) + \Psi(\dot{a})$, where $\Psi(\dot{a})$ is a dissipation

316 potential due to surface diffusion. A stationary value of Π with respect to $\dot{a}$

317 gives the solution that satisfies the constitute law for surface diffusion,

$$\delta\Pi \equiv \delta(\Delta\dot{G}) + \delta\Psi = 0. \tag{30}$$

318 The variation in change of Gibb's free energy, $\delta(\Delta\dot{G})$, with respect to a

319 variation $\delta\dot{a}$ is obtained from (28) as

$$\delta(\Delta\dot{G}) = \gamma_s A_s \left(\frac{2a\delta\dot{a}}{R_0^2} \right) \left(\xi_3\xi_4 + \frac{1}{4}(R_0 k)^2 + \frac{\tilde{\gamma}\xi_5 n \sin\omega_0}{\pi - n\omega_0} \right). \tag{31}$$

320 The dissipation potential $\Psi(\dot{a})$ is defined as

$$\Psi = \int_{A_s} \frac{j^2}{2\mathcal{D}_s} \, \mathrm{d}A_s, \tag{32}$$

321 where $\mathcal{D}_s = \delta_s D_s \Omega_s / (\mathrm{R}_G T)$ is the surface diffusion constant, δ_s is the thickness

322 over which surface diffusion occurs, D_s is the surface diffusivity, Ω_s is the

323 molar volume of the wire material, R_G is the universal gas constant, and

324 T is absolute temperature. To first order accuracy in a/R_0, we may write

325 $\mathrm{d}A_s = R_0 \, \mathrm{d}\varphi \, \mathrm{d}z$, so that (32) simplifies to

$$\Psi = \frac{nR_0}{\mathcal{D}_s} \int_0^\lambda \int_0^{\frac{\pi}{n} - \omega_0} j^2 \, \mathrm{d}\varphi \, \mathrm{d}z. \tag{33}$$

19

Now substitute the expression (17) for j into (33), and integrate to obtain

$$\Psi = \frac{\dot{a}^2 A_{\mathrm{s}}^0}{4 \mathcal{D}_{\mathrm{s}} k^2}. \tag{34}$$

Upon making use of (31) and (34), the variational statement (30) reduces to

$$\frac{\dot{a}}{a} = -\frac{4 \mathcal{D}_{\mathrm{s}} \gamma_{\mathrm{s}}}{R_0^4} (k R_0)^2 \left(\xi_3 \xi_4 + \frac{1}{4}(k R_0)^2 + \frac{\tilde{\gamma} \xi_5 n \sin \omega_0}{\pi - n \omega_0} \right) \tag{35}$$

for any assumed wavenumber k. The fastest growing perturbation has a wavelength that maximizes $\dot{a}$ in (35); by setting $\partial(\dot{a}/a)/(\partial k)$ to zero, the fastest growing wavelength is $\lambda_{\max} = \sqrt{2} \lambda_{\mathrm{c}}$, where λ_{c} has already been defined in (29). The wavenumber $k_{\max}$ that corresponds to $\lambda_{\max}$ follows immediately as

$$k_{\max} = \frac{\sqrt{2} \pi}{\lambda_{\max}} = \frac{k_c}{\sqrt{2}}, \tag{36}$$

and the fastest growth rate $(\dot{a}/a)_{\max}$ of the bundle at $\lambda = \lambda_{\max}$ follows directly from (35) as

$$\left(\frac{R_0^4}{\gamma_{\mathrm{s}} \mathcal{D}_{\mathrm{s}}} \frac{\dot{a}}{a} \right)_{\max} = (k_{\max} R_0)^4. \tag{37}$$

Note that the expression (36) for $k_{\max}$ is the same as that derived previously for the classical Rayleigh-Plateau instability of a single free-standing wire [21, 22].

20

5.3. Topology of wires after pinch-off

The wavelength of the fastest growing imperfection $\lambda_{\mathrm{max}} = \sqrt{2}\lambda_{\mathrm{c}}$ is given by (29) and can be written in the non-dimensional form $\tilde{\lambda}_{\mathrm{max}} = \lambda_{\mathrm{max}}/(2\pi R_0) = \sqrt{2}\tilde{\lambda}_{\mathrm{c}}$. The value of $\tilde{\lambda}_{\mathrm{max}}$ dictates the asymptotic shape of the final, pinched-off particles: (a) discrete sphere at small $\tilde{\lambda}_{\mathrm{max}}$, (b) truncated sphere at intermediate $\tilde{\lambda}_{\mathrm{max}}$, and (c) rod at large $\tilde{\lambda}_{\mathrm{max}}$. Consider each in turn.

(a) Discrete sphere

A small value of $\tilde{\lambda}_{\mathrm{max}}$ leads to break-up into an array of spherical droplets of final radius R_{s}. Conservation of mass dictates that

$$\frac{R_{\mathrm{s}}}{H} = \frac{1}{\cos\omega_0}\left(\frac{3}{2}\xi_1\tilde{\lambda}\right)^{1/3}. \tag{38}$$

This geometry occurs provided $R_{\mathrm{s}} < H$, and consequently $\tilde{\lambda}_{\mathrm{max}} < \tilde{\lambda}_1$, where

$$\tilde{\lambda}_1 \equiv \frac{2}{3}\frac{\cos^3\omega_0}{\xi_1} \tag{39}$$

upon suitable rearrangement of (38).

(b) Truncated sphere

Now consider the case $\tilde{\lambda}_{\mathrm{max}} > \tilde{\lambda}_1$. Then, the discrete droplets are truncated spheres with flat circular necks between immediate neighbors, see Fig. 7a. The height of each particle is $2H$, and its radius external to the necks is R_{s}. The radius of each neck is $R_{\mathrm{s}}\cos\omega_{\mathrm{s}}$, where $2\omega_{\mathrm{s}}$ is the angle subtended by the neck at the center of the particle. The radius R_{s} is related to R_0 via the

21

identity from (3):

$$H = R_\mathrm{s} \cos \omega_\mathrm{s} = R_0 \cos \omega_0 \tag{40}$$

once ω_s has been obtained from ω_0 by conservation of volume between the reference, unperturbed volume V_0 and the final volume of the truncated sphere. Routine algebra gives

$$V_0 = \xi_1 R_0^2 \lambda_\mathrm{max} = \frac{4}{3} \pi R_0^3 \xi_6 \cos^3 \omega_0, \tag{41}$$

where

$$\xi_6(\omega_\mathrm{s}, n) \equiv (\cos \omega_\mathrm{s})^{-3} \left(1 - \frac{n}{4} (2 + \cos \omega_\mathrm{s})(1 - \cos \omega_\mathrm{s})^2 \right). \tag{42}$$

A standard root-finding algorithm ("fzero" in Matlab R2021a) is used to solve (41) and (42) for ω_s in terms of $(n, \omega_0, \tilde{\lambda}_\mathrm{max})$. Truncated spheres are obtained for an intermediate value of $\tilde{\lambda}_\mathrm{max}$. When $\tilde{\lambda}_\mathrm{max}$ attains a transition value of $\tilde{\lambda}_2$, adjacent necks touch. This occurs at $n\omega_\mathrm{s} = 2\pi$, and the associated value of $\xi_6(\omega_\mathrm{s} = \frac{2\pi}{n}, n)$ is obtained from (42). Upon substitution into (41), we find

$$\tilde{\lambda}_2 = \frac{2 \cos^3 \omega_0}{3\xi_1(\omega_0, n)} \, \xi_6 \left(\frac{2\pi}{n}, n \right). \tag{43}$$

In summary, truncated spheres are the pinched-off final shape when $\tilde{\lambda}_1 < \tilde{\lambda}_\mathrm{max} < \tilde{\lambda}_2$.

22

(c) Rods

The discrete droplets adopt a rod-like shape for $\tilde{\lambda}_{max} > \tilde{\lambda}_2$, as shown in
Fig. 7a.

5.4. Pinch-off time

Our linear perturbation analysis describes the initial stage of shape evolu-
tion. It does not accurately capture the details of the nanowire pinch-off into
discrete spheres. However, previous numerical calculations have shown that
the initial perturbation growth rate is a good predictor for the pinch-off time
[25]. Assume that a nanowire of initial perturbation amplitude a_I at time t_I
pinches off when the perturbation amplitude reaches a value a_p at time t_p.
The pinch-off time t_p is related to the perturbation growth rate $\dot{a}(t_I)$ via the
approximation [25],

$$\ln\left(\frac{a_p}{a_I}\right) = \int_{t_I}^{t_p} \frac{\dot{a}}{a}(t')\, dt' \approx (t_p - t_I)\frac{\dot{a}}{a}(t_I). \tag{44}$$

By setting $t_I = 0$ and inserting the fastest growth rate from (37), the pinch-off
time is predicted as

$$\frac{\gamma_s \mathcal{D}_s t_p}{R_0^4} = (k_{max} R_0)^{-4} \ln\left(\frac{a_p}{a_I}\right), \tag{45}$$

which is again consistent with the results obtained by Nichols and Mullins
[22] for an isolated metal nanowire. Note that $k_{max} = 2\pi/\lambda_{max}$ is directly
related to $k_c = 2\pi/\lambda_c$ via (36) and consequently $k_{max} = \sqrt{2}\pi/\lambda_c$. Also
recall that $\tilde{\lambda}_c = \lambda_c/(2\pi R_0)$ is a function of $(n, \tilde{\gamma}, \omega_0)$ as given by (29) and
Fig. 6. Assume that all wavelengths of perturbation are present in the wire

23

so that the pinch-off time is dictated by the fastest growing perturbation of wavelength $\lambda_{\max} = \sqrt{2}\lambda_{\mathrm{c}}$. Thus, upon making use of (45), the pinch-off time t_{p} scales as $\tilde{\lambda}_{\mathrm{c}}^4$; some broad conclusions can be deduced immediately from Fig. 6. Consider a close-packed, fully triangulated arrangement of wires ($n = 6$), with $\tilde{\gamma} < 0.8$. Then, pinch-off is fastest for small contacts ($\omega_0 \approx 0$) corresponding to low relative density and for large contacts ($\omega_0 \approx \pi/6$) corresponding to almost vanishing porosity. A large drop in surface energy from the surface value γ_{s} to the interfacial, contact value γ_{c} (that is, a small value of $\tilde{\gamma} \equiv \gamma_{\mathrm{c}}/\gamma_{\mathrm{s}}$) leads to a faster pinch-off.

The formula (45) also applies to the case of a free-standing wire, with $k_{\max} = \sqrt{2}\pi/\lambda_{\mathrm{c}}$ and $\lambda_{\mathrm{c}} = 2\pi R_0$, such that $\tilde{\lambda}_{\mathrm{c}} = 1$. Thus, the plots of Fig. 6 can be used immediately to determine whether bundling reduces or increases pinch-off time. In broad terms, a bundle of wires is more stable than the isolated wire in regimes of the map for which $\tilde{\lambda}_{\mathrm{c}} > 1$.

6. Discussion

6.1. Comparison of experiment and perturbation analysis

The experiments reported above indicate that a bundle of ultrathin gold nanowires fragments more slowly than freely dispersed nanowires. Our perturbation analysis shows that stabilization arises from the presence of necks between wires. Whether stabilization occurs or not depends upon the number of necks n, surface energy ratio $\tilde{\gamma}$, and initial contact angle ω_0 as shown in the stability maps of Fig. 6. It is instructive to make use of the material properties and geometric parameters of the present experimental study in order to assess whether the predictions match the observed stabilization due

24

to bundle formation.

The measured radius of gold nanowires was approximately $0.84\,\mathrm{nm}$ and the thickness of the ligand shell was $2.2\,\mathrm{nm}$ [54, 55]. The AuNWs formed fully-triangulated bundles with $n = 6$ and a center-to-center distance of $5.7\,\mathrm{nm}$, giving $\omega_0 \approx \pi/10$. The surface energy γ_s is set by the interaction between ligand and solvent molecules, and the interfacial energy γ_c by the interaction of ligand shells. The spacing indicates that solvent was always present between the ligand shells, implying $\tilde{\gamma} \approx 1$. These parameters put the system at the operating point $(n, \tilde{\gamma}, n\omega_0/\pi) \approx (6, 1, 0.6)$ in the maps of Fig. 6, inside a region of unconditional stability. This explains why the bundled AuNWs were observed to be more stable than the freely dispersed ones.

Nouh et al. [40] exchanged the ligand oleylamine with trioctylphosphine and observed that the wires' stability increased, but did not provide an explanation for this finding. It was not stated whether stabilization was due to the different bond chemistry, the steric properties of the ligands, or the tighter bundling at an interwire distance of $3.75\,\mathrm{nm}$ [40]. We locate their material and geometric parameters to be at the operating point $(n, \tilde{\gamma}, n\omega_0/\pi) \approx (6, 1, 0.8)$ in Fig. 6 in a region of unconditional stability, consistent with their experimental observations.

6.2. Comparison of pinch-off time and free sintering time

The analysis of the Rayleigh-Plateau pinch-off instability of a bundle of wires assumes that the center-to-center spacing of the wires remains constant, with the instability driven by surface diffusion in the axial direction. In addition, free sintering can occur such that the bundle of wires densifies by in-plane

25

surface diffusion, and the center-to-center spacing of neighboring nanowires reduces. It is instructive to obtain an expression for the sintering time t_s to achieve a given contact size c between adjoining wires, and to compare this sintering time with the pinch-off time t_p for this same value of c. Sintering stabilizes against pinch-off when t_s is less than t_p. Alternatively, when t_s exceeds t_p the Rayleigh-Plateau instability occurs with break-up of the wires into discrete particles.

The sintering time t_s is calculated as follows. We focus attention on the early stages of sintering involving initial neck formation and neck growth (stage I sintering) [56, 51]. Consider a row of cylinders with an initial contact length $c = 0$ (see Fig. A.1). Sintering increases c and decreases H, as shown in Fig. A.1. We follow Parhami et al. [51] and determine, for the 2D plane strain case, the dependence of c upon sintering time t_s, such that

$$c^6 = \frac{81}{2}\mathcal{D}_c R_0^2(2\gamma_s - \gamma_c)t_s. \tag{46}$$

Here, $\mathcal{D}_c$ is the diffusion constant in the contact zone (grain boundary). The derivation is given in Appendix A.

The sintering time t_s to achieve a neck size c is compared in Fig. 8 with the pinch-off time t_p for the same value of c, for selected values of $\tilde{\gamma}$ and $\tilde{D} = \mathcal{D}_c/\mathcal{D}_s$. Sintering is sufficiently fast to stabilize the nanowire shape at large $\tilde{\gamma}$ and large $\tilde{D}$. These conditions are typically satisfied for metals, for which $\tilde{\gamma} \approx 0.3$ to 0.4 [57] and $\tilde{D} \approx 10^{-3}$ to 10^{-1} [58]. Note that, for the choice $\tilde{\gamma} = 0.1$ and $\tilde{D} = 10^{-5}$, pinch-off is anticipated at $c/R_0 \approx 0.1$ since $t_p = t_s$ at this value of contact size between neighboring wires.

A critical neck size c_c can be defined for which $t_s = t_p$. Then, the sintering

26

time is smaller than the pinch-off time for $c < c_c$. For $c > c_c$, the instability is faster than sintering and the wires break up into discrete droplets. Contours of c_c are plotted in Fig. 9: c_c increases with increasing relative diffusivity $\tilde{D}$. For sufficiently large $\tilde{D}$, sintering is always faster than pinch-off and thereby stabilizes the wire.

7. Concluding remarks

Ultrathin nanowires can self-assemble into bundles. *In situ* SAXS and *ex situ* TEM reveal that bundling delays the Rayleigh-Plateau instability. An analytical model, based on interfacial energy, geometrical confinement and axial surface diffusion, indicates that bundle formation can render the nanowire unconditionally stable. Stability depends upon the number and size of necks between neighboring wires, and upon the surface and interfacial energies. An optimal neck size maximizes pinch-off time for packings with more than two neighbors.

Pressureless sintering, in its early stages, is much more rapid than the rate of pinch-off by the Rayleigh-Plateau instability. However, the rate of sintering decreases sharply with increasing time, $\dot{c} \propto t^{-5/6}$ as given directly from (46), and consequently the Rayleigh-Plateau instability may ensue.

27

References

[1] L. Cademartiri, G. A. Ozin, Ultrathin Nanowires-A Materials Chemistry Perspective, Advanced Materials 21 (2009) 1013–1020. URL: http://doi.wiley.com/10.1002/adma.200801836. doi:10.1002/adma.200801836.

[2] J. Gao, C. M. Bender, C. J. Murphy, Dependence of the Gold Nanorod Aspect Ratio on the Nature of the Directing Surfactant in Aqueous Solution, Langmuir 19 (2003) 9065–9070. URL: http://pubs.acs.org/doi/abs/10.1021/la034919i. doi:10.1021/la034919i.

[3] N. Pazos-Pérez, D. Baranov, S. Irsen, M. Hilgendorff, L. M. Liz-Marzán, M. Giersig, Synthesis of Flexible, Ultrathin Gold Nanowires in Organic Media, Langmuir 24 (2008) 9855–9860. URL: http://pubs.acs.org/doi/abs/10.1021/la801675d. doi:10.1021/la801675d.

[4] T. K. Sau, A. L. Rogach, Nonspherical Noble Metal Nanoparticles: Colloid-Chemical Synthesis and Morphology Control, Advanced Materials 22 (2010) 1781–1804. URL: https://onlinelibrary.wiley.com/doi/10.1002/adma.200901271. doi:10.1002/adma.200901271.

[5] H. You, X. Liu, H. Liu, J. Fang, Theoretical description of the role of amine surfactant on the anisotropic growth of gold nanocrystals, CrystEngComm 18 (2016) 3934–3941. URL: http://xlink.rsc.org/?DOI=C6CE00550K. doi:10.1039/C6CE00550K.

[6] M. J. Kim, S. Alvarez, Z. Chen, K. A. Fichthorn, B. J. Wiley, Single-Crystal Electrochemistry Reveals Why Metal Nanowires Grow, Journal of the American Chemical Society 140 (2018) 14740–14746. URL: http://pubs.acs.org/doi/10.1021/jacs.

28

510   8b08053https://pubs.acs.org/doi/10.1021/jacs.8b08053. doi:10.
511   1021/jacs.8b08053.

[7]   A. Halder, N. Ravishankar, Ultrafine Single-Crystalline Gold Nanowire
       Arrays by Oriented Attachment, Advanced Materials 19 (2007) 1854–
       1858. URL: https://onlinelibrary.wiley.com/doi/10.1002/adma.
       200602325. doi:10.1002/adma.200602325.

[8]   Z. Huo, C.-k. Tsung, W. Huang, X. Zhang, P. Yang, Sub-Two Nanome-
       ter Single Crystal Au Nanowires, Nano Letters 8 (2008) 2041–2044.
       URL: https://pubs.acs.org/doi/10.1021/nl8013549. doi:10.1021/
       nl8013549.

[9]   C. Wang, Y. Hu, C. M. Lieber, S. Sun, Ultrathin Au Nanowires
       and Their Transport Properties, Journal of the American Chemical
       Society 130 (2008) 8902–8903. URL: https://pubs.acs.org/doi/10.
       1021/ja803408f. doi:10.1021/ja803408f.

[10]   X. Lu, M. S. Yavuz, H.-y. Tuan, B. A. Korgel, Y. Xia, Ultrathin
       Gold Nanowires Can Be Obtained by Reducing Polymeric Strands
       of Oleylamine-AuCl Complexes Formed via Aurophilic Interaction,
       Journal of the American Chemical Society 130 (2008) 8900–8901.
       URL: https://pubs.acs.org/doi/10.1021/ja803343m. doi:10.1021/
       ja803343m.

[11]   C. Wang, Y. Hou, J. Kim, S. Sun, A General Strategy for Synthesiz-
       ing FePt Nanowires and Nanorods, Angewandte Chemie International
       Edition 46 (2007) 6333–6335. URL: http://doi.wiley.com/10.1002/
       anie.200702001. doi:10.1002/anie.200702001.

[12]   B. Li, S. Ye, I. E. Stewart, S. Alvarez, B. J. Wiley, Synthesis and
       Purification of Silver Nanowires To Make Conducting Films with a
       Transmittance of 99%, Nano Letters 15 (2015) 6722–6726. URL:
       http://pubs.acs.org/doi/10.1021/acs.nanolett.5b02582. doi:10.
       1021/acs.nanolett.5b02582.

[13]   W. Zhao, D. Huang, Q. Yuan, X. Wang, Sub-2.0-nm Ru
       and composition-tunable RuPt nanowire networks, Nano Research
       9 (2016) 3066–3074. URL: http://link.springer.com/10.1007/
       s12274-016-1189-4. doi:10.1007/s12274-016-1189-4.

29

[14] Z. Liu, D. Xu, J. Liang, J. Shen, S. Zhang, Y. Qian, Growth of Cu 2 S Ultrathin Nanowires in a Binary Surfactant Solvent, The Journal of Physical Chemistry B 109 (2005) 10699–10704. URL: `http://pubs.acs.org/doi/abs/10.1021/jp050332w`. doi:10.1021/jp050332w.

[15] L. Cademartiri, R. Malakooti, P. G. O'Brien, A. Migliori, S. Petrov, N. P. Kherani, G. A. Ozin, Large-Scale Synthesis of Ultrathin Bi2S3 Necklace Nanowires, Angewandte Chemie International Edition 47 (2008) 3814–3817. URL: `http://doi.wiley.com/10.1002/anie.200705034`. doi:10.1002/anie.200705034.

[16] R. Malakooti, L. Cademartiri, A. Migliori, G. A. Ozin, Ultrathin Sb 2 S 3 nanowires and nanoplatelets, J. Mater. Chem. 18 (2008) 66–69. URL: `http://xlink.rsc.org/?DOI=B713383A`. doi:10.1039/B713383A.

[17] S. Gong, Y. Zhao, Q. Shi, Y. Wang, L. W. Yap, W. Cheng, Self-assembled Ultrathin Gold Nanowires as Highly Transparent, Conductive and Stretchable Supercapacitor, Electroanalysis 28 (2016) 1298–1304. doi:10.1002/elan.201600081.

[18] J. H. M. Maurer, L. González-García, B. Reiser, I. Kanelidis, T. Kraus, Templated Self-Assembly of Ultrathin Gold Nanowires by Nanoimprinting for Transparent Flexible Electronics, Nano Letters 16 (2016) 2921–2925. URL: `http://pubs.acs.org/doi/10.1021/acs.nanolett.5b04319`. doi:10.1021/acs.nanolett.5b04319.

[19] A. Loubat, M. Impéror-Clerc, B. Pansu, F. Meneau, B. Raquet, G. Viau, L.-M. Lacroix, Growth and Self-Assembly of Ultrathin Au Nanowires into Expanded Hexagonal Superlattice Studied by in Situ SAXS, Langmuir 30 (2014) 4005–4012. URL: `https://pubs.acs.org/doi/10.1021/la500549z`. doi:10.1021/la500549z.

[20] B. Y. Xia, H. B. Wu, Y. Yan, X. W. D. Lou, X. Wang, Ultrathin and Ultralong Single-Crystal Platinum Nanowire Assemblies with Highly Stable Electrocatalytic Activity, Journal of the American Chemical Society 135 (2013) 9480–9485. URL: `https://pubs.acs.org/doi/10.1021/ja402955t`. doi:10.1021/ja402955t.

[21] F. A. Nichols, W. W. Mullins, Morphological Changes of a Surface of Revolution due to Capillarity-Induced Surface Diffusion, Journal of

30

Applied Physics 36 (1965) 1826–1835. URL: `http://aip.scitation.org/doi/10.1063/1.1714360`. doi:`10.1063/1.1714360`.

[22] F. A. Nichols, W. W. Mullins, Surface- (interface-) and volume diffusion contributions to morphological changes driven by capillarity, AIME Metallurgical Society Transactions 233 (1965) 1840–1848. URL: `http://www.onemine.org/document/abstract.cfm?docid=26784`.

[23] J. A. F. Plateau, Statique experimentale et theorique des liquides soumis aux seules forces moleculaires, Gauthiers-Villars, Paris, 1873.

[24] L. Rayleigh, On The Instability Of Jets, Proceedings of the London Mathematical Society s1-10 (1878) 4–13. URL: `http://doi.wiley.com/10.1112/plms/s1-10.1.4`. doi:`10.1112/plms/s1-10.1.4`.

[25] S. Bettscheider, T. Kraus, N. A. Fleck, On the geometric stability of an inorganic nanowire and an organic ligand shell, Journal of the Mechanics and Physics of Solids 123 (2019) 3–19. URL: `https://linkinghub.elsevier.com/retrieve/pii/S0022509618305830`. doi:`10.1016/j.jmps.2018.07.017`. arXiv:`1808.01011`.

[26] M. S. McCallum, P. W. Voorhees, M. J. Miksis, S. H. Davis, H. Wong, Capillary instabilities in solid thin films: Lines, Journal of Applied Physics 79 (1996) 7604–7611. URL: `http://aip.scitation.org/doi/10.1063/1.362343`. doi:`10.1063/1.362343`.

[27] K. F. Gurski, G. B. McFadden, M. J. Miksis, The Effect of Contact Lines on the Rayleigh Instability with Anisotropic Surface Energy, SIAM Journal on Applied Mathematics 66 (2006) 1163–1187. URL: `http://epubs.siam.org/doi/10.1137/050626946`. doi:`10.1137/050626946`.

[28] S. P. A. Gill, Controlling the Rayleigh instability of nanowires, Applied Physics Letters 102 (2013) 143108. URL: `http://aip.scitation.org/doi/10.1063/1.4801766`. doi:`10.1063/1.4801766`.

[29] G. Boussinot, E. A. Brener, Inhibition of Rayleigh-Plateau instability on a unidirectionally patterned substrate, Physical Review E 92 (2015) 032408. URL: `https://link.aps.org/doi/10.1103/PhysRevE.92.032408`. doi:`10.1103/PhysRevE.92.032408`.

31

[30] J. Cahn, Stability of rods with anisotropic surface free energy, Scripta Metallurgica 13 (1979) 1069–1071. URL: `http://linkinghub.elsevier.com/retrieve/pii/0036974879902059`. doi:`10.1016/0036-9748(79)90205-9`.

[31] A. M. Glaeser, Model Studies of Rayleigh Instabilities via Microdesigned Interfaces, Interface Science 9 (2001) 65–82. URL: `http://link.springer.com/10.1023/A:1011279015039`. doi:`10.1023/A:1011279015039`.

[32] K. F. Gurski, G. B. McFadden, The effect of anisotropic surface energy on the Rayleigh instability, Proceedings of the Royal Society A: Mathematical, Physical and Engineering Sciences 459 (2003) 2575–2598. URL: `http://rspa.royalsocietypublishing.org/cgi/doi/10.1098/rspa.2003.1144`. doi:`10.1098/rspa.2003.1144`.

[33] G. H. Kim, C. V. Thompson, Effect of surface energy anisotropy on Rayleigh-like solid-state dewetting and nanowire stability, Acta Materialia 84 (2015) 190–201. URL: `http://linkinghub.elsevier.com/retrieve/pii/S1359645414007800`. doi:`10.1016/j.actamat.2014.10.028`.

[34] Y. Imura, S. Hojo, C. Morita, T. Kawai, Preparation of Silica-Coated Ultrathin Gold Nanowires with High Morphological Stability, Langmuir 30 (2014) 1888–1892. URL: `https://pubs.acs.org/doi/10.1021/la403681w`. doi:`10.1021/la403681w`.

[35] S. P. O. Danielsen, J. Choi, R. J. Composto, Retardation of shape change of Au nanorods using photo-cross-linkable ligands, Journal of Polymer Science Part B: Polymer Physics 54 (2016) 301–307. URL: `https://onlinelibrary.wiley.com/doi/10.1002/polb.23929`. doi:`10.1002/polb.23929`.

[36] W. J. Kennedy, S. Izor, B. D. Anderson, G. Frank, V. Varshney, G. J. Ehlert, Thermal Reshaping Dynamics of Gold Nanorods: Influence of Size, Shape, and Local Environment, ACS Applied Materials & Interfaces 10 (2018) 43865–43873. URL: `https://pubs.acs.org/doi/10.1021/acsami.8b12965`. doi:`10.1021/acsami.8b12965`.

[37] Y. Imura, H. Tanuma, H. Sugimoto, R. Ito, S. Hojo, H. Endo, C. Morita, T. Kawai, Water-dispersible ultrathin Au nanowires prepared using a lamellar template of a long-chain amidoamine derivative, Chemical Communications 47 (2011) 6380. URL: `http://xlink.rsc.org/?DOI=c0cc05545j`. doi:`10.1039/c0cc05545j`.

[38] S. E. Huber, C. Warakulwit, J. Limtrakul, T. Tsukuda, M. Probst, Thermal stabilization of thin gold nanowires by surfactant-coating: a molecular dynamics study, Nanoscale 4 (2012) 585–590. URL: `http://xlink.rsc.org/?DOI=C1NR11282A`. doi:`10.1039/C1NR11282A`.

[39] R. Takahata, S. Yamazoe, C. Warakulwit, J. Limtrakul, T. Tsukuda, Rayleigh Instability and Surfactant-Mediated Stabilization of Ultrathin Gold Nanorods, The Journal of Physical Chemistry C 120 (2016) 17006–17010. URL: `https://pubs.acs.org/doi/10.1021/acs.jpcc.6b03113`. doi:`10.1021/acs.jpcc.6b03113`.

[40] E. S. A. Nouh, E. A. Baquero, L.-M. Lacroix, F. Delpech, R. Poteau, G. Viau, Surface-Engineering of Ultrathin Gold Nanowires: Tailored Self-Assembly and Enhanced Stability, Langmuir 33 (2017) 5456–5463. URL: `https://pubs.acs.org/doi/10.1021/acs.langmuir.7b00477`. doi:`10.1021/acs.langmuir.7b00477`.

[41] B. Reiser, D. Gerstner, L. Gonzalez-Garcia, J. H. M. Maurer, I. Kanelidis, T. Kraus, Multivalent bonds in self-assembled bundles of ultrathin gold nanowires, Physical Chemistry Chemical Physics 18 (2016) 27165–27169. URL: `http://xlink.rsc.org/?DOI=C6CP05181B`. doi:`10.1039/C6CP05181B`.

[42] S. Bettscheider, B. Kuttich, L. F. Engel, L. González-García, T. Kraus, Bundling of Nanowires Induced by Unbound Ligand, The Journal of Physical Chemistry C 125 (2021) 3590–3598. URL: `https://pubs.acs.org/doi/10.1021/acs.jpcc.0c10919`. doi:`10.1021/acs.jpcc.0c10919`.

[43] H. Gao, S. Bettscheider, T. Kraus, M. H. Müser, Entropy Can Bundle Nanowires in Good Solvents, Nano Letters 19 (2019) 6993–6999. URL: `https://pubs.acs.org/doi/10.1021/acs.nanolett.9b02379`. doi:`10.1021/acs.nanolett.9b02379`.

[44] J. H. M. Maurer, L. González-García, B. Reiser, I. Kanelidis, T. Kraus, Sintering of Ultrathin Gold Nanowires for Transparent Electronics, ACS Applied Materials & Interfaces 7 (2015) 7838–7842. URL: `https://pubs.acs.org/doi/10.1021/acsami.5b02088`. doi:10.1021/`acsami.5b02088`.

[45] H. Feng, Y. Yang, Y. You, G. Li, J. Guo, T. Yu, Z. Shen, T. Wu, B. Xing, Simple and Rapid Synthesis of Ultrathin Gold Nanowires, their Self-Assembly and Application in Surface-Enhanced Raman Scattering, Chemical Communications 0 (2009) 1984. URL: `http://xlink.rsc.org/?DOI=b822507a`. doi:10.1039/b822507a.

[46] S. Förster, A. Timmann, M. Konrad, C. Schellbach, A. Meyer, S. S. Funari, P. Mulvaney, R. Knott, Scattering Curves of Ordered Mesoscopic Materials, Journal of Physical Chemistry B 109 (2005) 1347–1360. URL: `http://pubs.acs.org/doi/abs/10.1021/jp0467494`. doi:10.1021/jp0467494.

[47] A. Sundblom, C. L. P. Oliveira, A. E. C. Palmqvist, J. S. Pedersen, Modeling in Situ Small-Angle X-ray Scattering Measurements Following the Formation of Mesostructured Silica, The Journal of Physical Chemistry C 113 (2009) 7706–7713. URL: `https://pubs.acs.org/doi/10.1021/jp809798c`. doi:10.1021/jp809798c.

[48] S. Manet, J. Schmitt, M. Impéror-Clerc, V. Zholobenko, D. Durand, C. L. P. Oliveira, J. S. Pedersen, C. Gervais, N. Baccile, F. Babonneau, I. Grillo, F. Meneau, C. Rochas, Kinetics of the Formation of 2D-Hexagonal Silica Nanostructured Materials by Nonionic Block Copolymer Templating in Solution, The Journal of Physical Chemistry B 115 (2011) 11330–11344. URL: `https://pubs.acs.org/doi/10.1021/jp200213k`. doi:10.1021/jp200213k.

[49] M. Newville, R. Otten, A. Nelson, A. Ingargiola, T. Stensitzki, D. Allan, A. Fox, F. Carter, Michał, D. Pustakhod, Lneuhaus, S. Weigand, R. O. Glenn, C. D. Mark, A. L. R. Hansen, G. Pasquevich, L. Foks, N. Zobrist, O. Frost, A. Beelen, Stuermer, Kwertyops, A. Polloreno, S. Caldwell, A. Almarza, A. Persaud, B. Gamari, B. F. Maier, lmfit, 2021. URL: `https://zenodo.org/record/4516651`. doi:10.5281/`zenodo.4516651`.

[50] M. Saitoh, Y. Kashiwagi, M. Chigane, Structural Analysis of Micrometer-Long Gold Nanowires Using a Wormlike Chain Model and Their Rheological Properties, Soft Matter 13 (2017) 3927–3935. URL: `http://xlink.rsc.org/?DOI=C7SM00284J`. doi:10.1039/C7SM00284J.

[51] F. Parhami, R. McMeeking, A. Cocks, Z. Suo, A model for the sintering and coarsening of rows of spherical particles, Mechanics of Materials 31 (1999) 43–61. URL: `https://linkinghub.elsevier.com/retrieve/pii/S0167663698000490`. doi:10.1016/S0167-6636(98)00049-0.

[52] A. J. R. Hensley, K. Ghale, C. Rieg, T. Dang, E. Anderst, F. Studt, C. T. Campbell, J.-S. McEwen, Y. Xu, DFT-Based Method for More Accurate Adsorption Energies: An Adaptive Sum of Energies from RPBE and vdW Density Functionals, The Journal of Physical Chemistry C 121 (2017) 4937–4945. URL: `https://pubs.acs.org/doi/10.1021/acs.jpcc.6b10187`. doi:10.1021/acs.jpcc.6b10187.

[53] A. C. F. Cocks, S. P. A. Gill, J. Pan, Modeling Microstructure Evolution in Engineering Materials, in: E. van der Giessen, T. Wu (Eds.), Advances in Applied Mechanics Volume 36, Academic Press, 1998, pp. 82–162. URL: `https://www.elsevier.com/books/advances-in-applied-mechanics/unknown/978-0-12-002036-2`.

[54] J. Borges, J. A. Ribeiro, E. M. Pereira, C. A. Carreira, C. M. Pereira, F. Silva, Preparation and characterization of DNA films using oleylamine modified Au surfaces, Journal of Colloid and Interface Science 358 (2011) 626–634. doi:10.1016/j.jcis.2011.03.039.

[55] S. Mourdikoudis, L. M. Liz-Marzán, Oleylamine in Nanoparticle Synthesis, Chemistry of Materials 25 (2013) 1465–1476. URL: `https://pubs.acs.org/doi/10.1021/cm4000476`. doi:10.1021/cm4000476.

[56] R. L. Coble, Initial Sintering of Alumina and Hematite, Journal of the American Ceramic Society 41 (1958) 55–62. URL: `https://onlinelibrary.wiley.com/doi/10.1111/j.1151-2916.1958.tb13519.x`. doi:10.1111/j.1151-2916.1958.tb13519.x.

[57] T. Roth, The surface and grain boundary energies of iron, cobalt and nickel, Materials Science and Engineering 18 (1975) 183–192. URL: `https://linkinghub.elsevier.com/retrieve/pii/`

739   0025541675901627https://linkinghub.elsevier.com/retrieve/
740   pii/0025541675901688. doi:10.1016/0025-5416(75)90168-8.

741 [58] T. Wejrzanowski, K. J. Kurzydlowski,   Modeling of Size Ef-
742   fects in Diffusion Driven Processes at Nanoscale - Large Atomic
743   and Mesoscale Methods,   Diffusion Foundations 12 (2017) 38–
744   73. URL: https://www.scientific.net/DF.12.38. doi:10.4028/www.
745   scientific.net/DF.12.38.

36

746

747

748

749

750

751

752

753

754
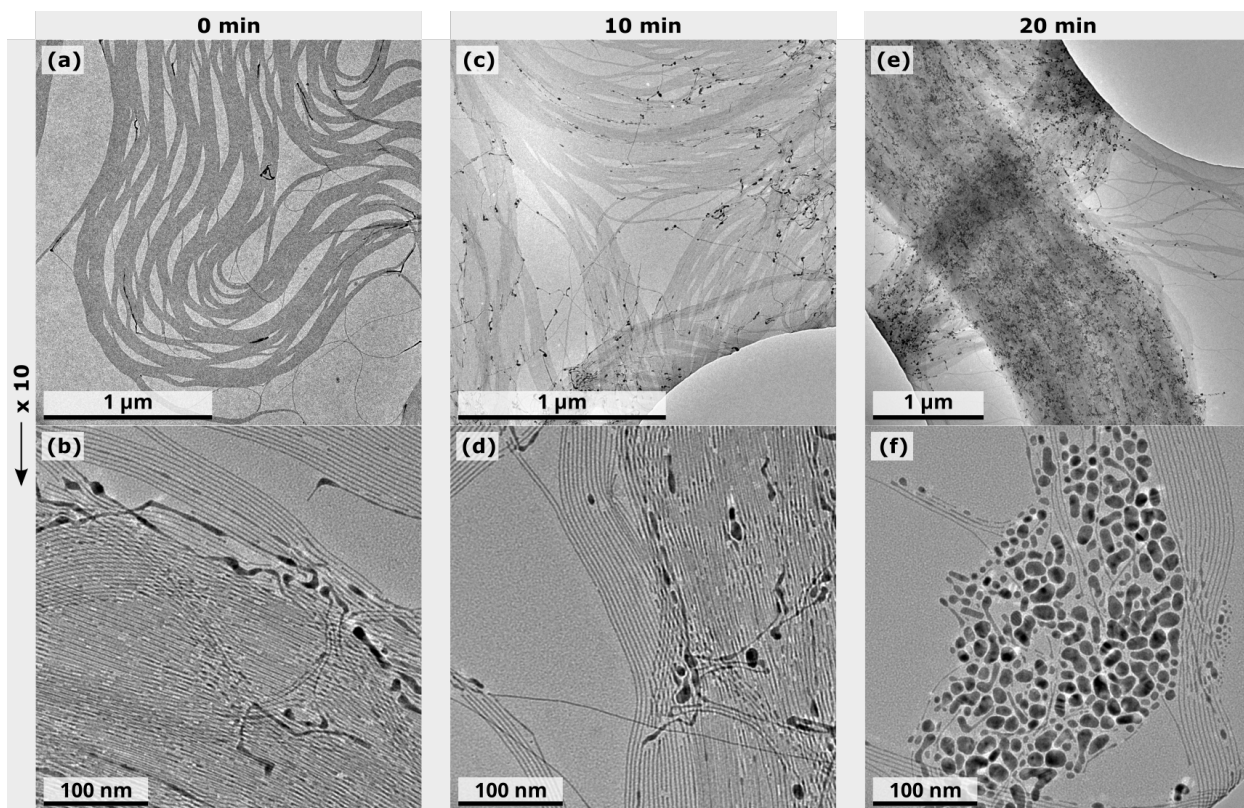
Figure 1: Transmission electron micrographs of ultrathin gold nanowires after drying at room temperature **(a)** and **(b)**; and after heating them to 60 °C for 10 min **(c)** and **(d)**; and 20 min **(e)** and **(f)**. The wires fragmented into spherical particles.
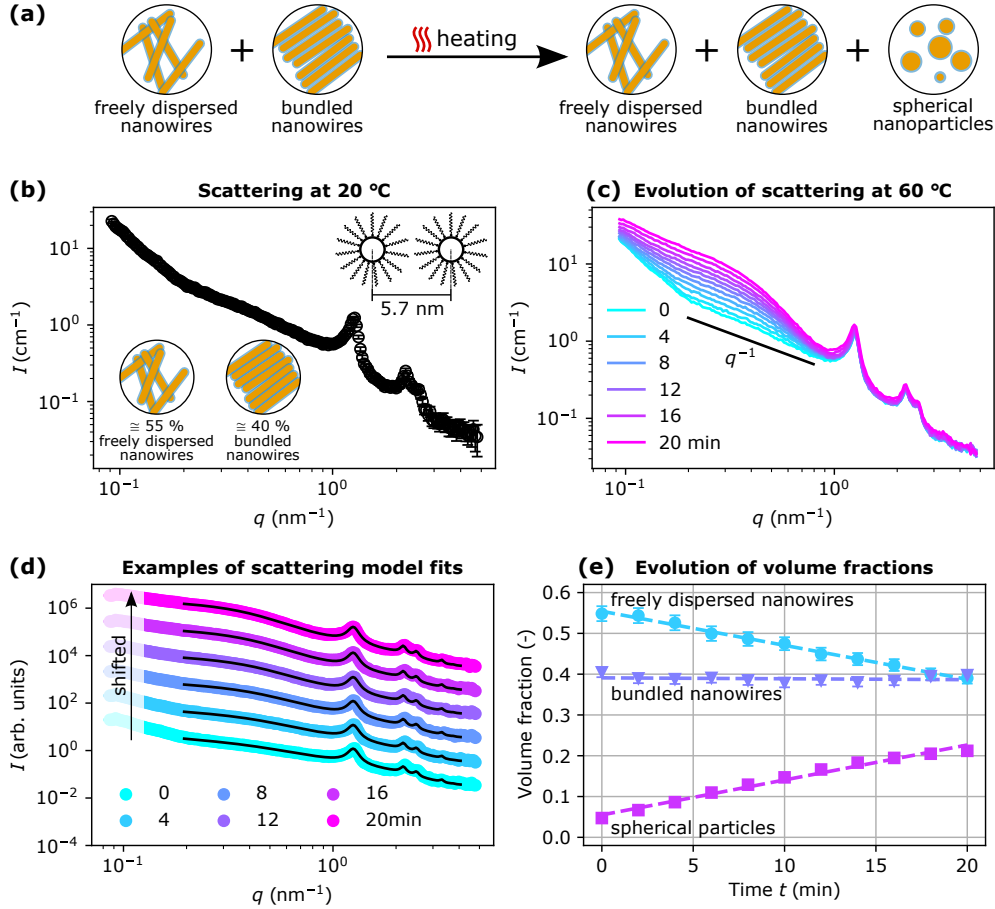
Figure 2: Analysis of nanowire shape stability via X-ray scattering. **(a)** The fragmentation of wires was induced by heating a dispersion to 60 °C and was observed via *in situ* Small-Angle X-rax Scattering (SAXS). **(b)** Distinct scattering maxima indicate that 40 % of the gold existed in bundles and 55 % in dispersed nanowires. The remaining 5 % were in spherical nanoparticles, a by-product of the synthesis. The interwire (center to center) distance inside the bundles was 5.7 nm.**(c)** Heating to 60 °C increased scattering at small q-values, indicating the formation of spheres. **(d)** Scattering models (solid lines) were fitted to the scattering (dots) at selected times to quantify the change in volume fractions. The scattering curves are shifted vertically for better visualization. **(e)** Volume fractions of gold in freely dispersed nanowires, bundled nanowires, and spherical particles from the scattering models. Error bars denote the standard errors of the fits. The dashed line are linear fits.
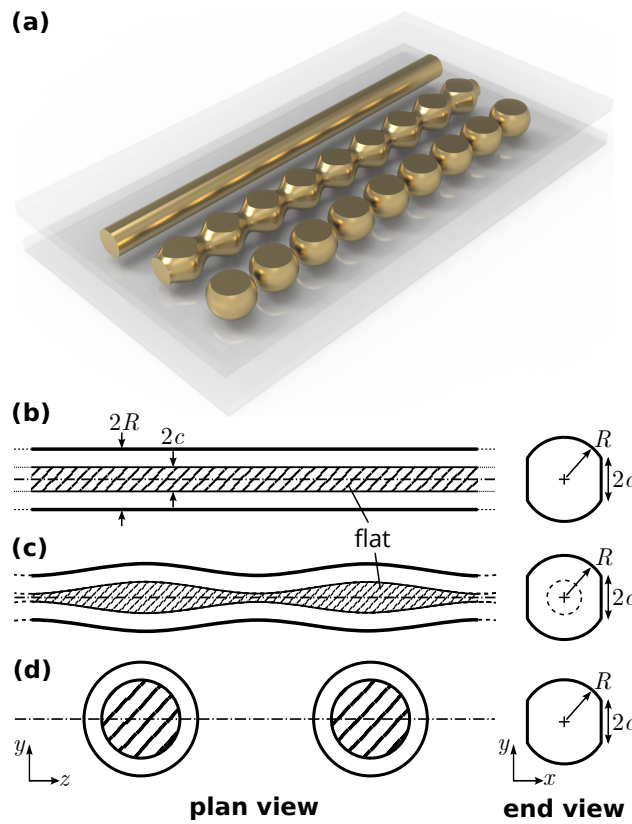
Figure 3: The prototypical problem showing a stacked nanowire. **(a)** Rendered view of three states. The nanowire may remain **(b)** prismatic in shape (stable), or it may evolve into **(c)** a non-uniform shape and thence to **(d)** discrete droplets.
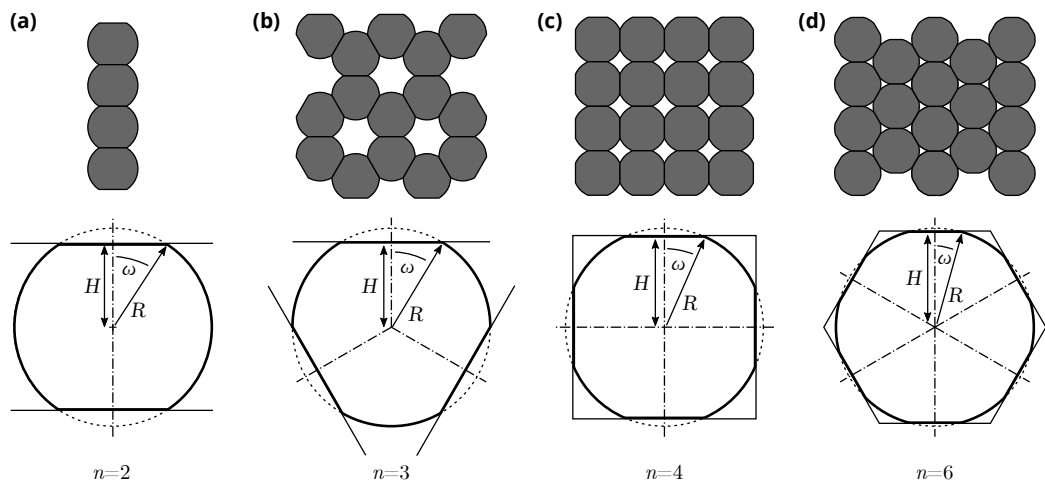
Figure 4: Geometry of a nanowire truncated by $n = 2, 3, 4$, or 6 flat surfaces that represent necks of neighboring wires. **(a)** $n = 2$, **(b)** $n = 3$, **(c)** $n = 4$, **(d)** $n = 6$.
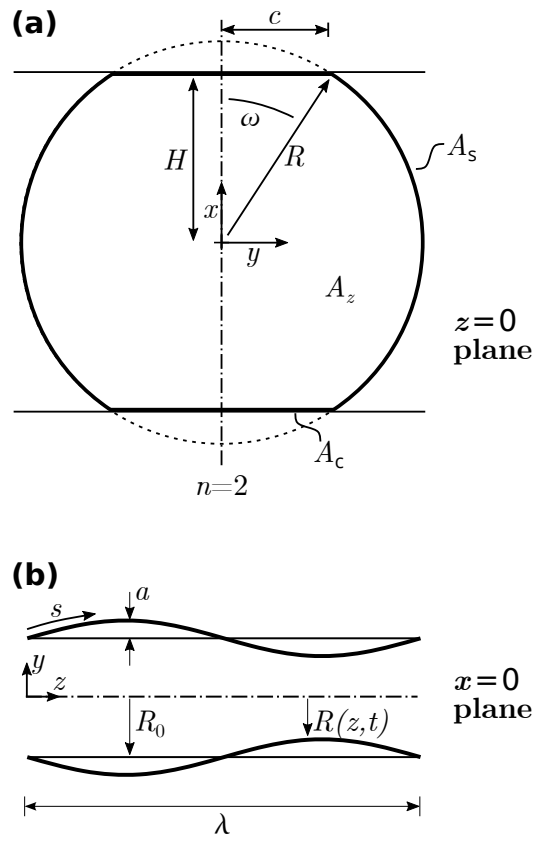
Figure 5: Cylindrical coordinate system and geometry of a perturbed nanowire. **(a)** The (x, y)-plane and **(b)** the (y, z)-plane (**B**).
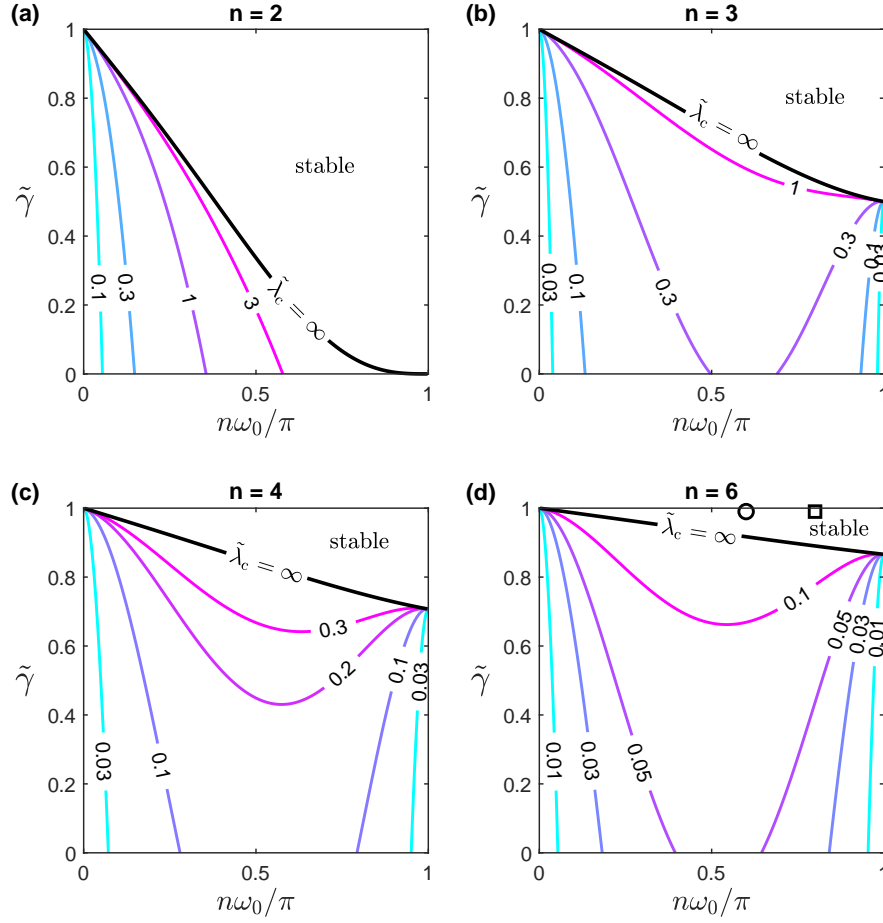
Figure 6: Contours of the critical perturbation wavelength $\tilde{\lambda}_c = \lambda_c/(2\pi R_0)$ as a function of the surface energies $\tilde{\gamma}$ and the initial contact angle ω_0 for a cylinder constrained by **(a)** $n = 2$, **(b)** $n = 3$, **(c)** $n = 4$, and **(d)** $n = 6$ necks. The black line separates the regime in which shape stability depends on the perturbation wavelength from the regime in which the cylinder is always stable regardless of the perturbation wavelength. The circle locates our experimental material and system properties and the square that of Nouh et al. [40].
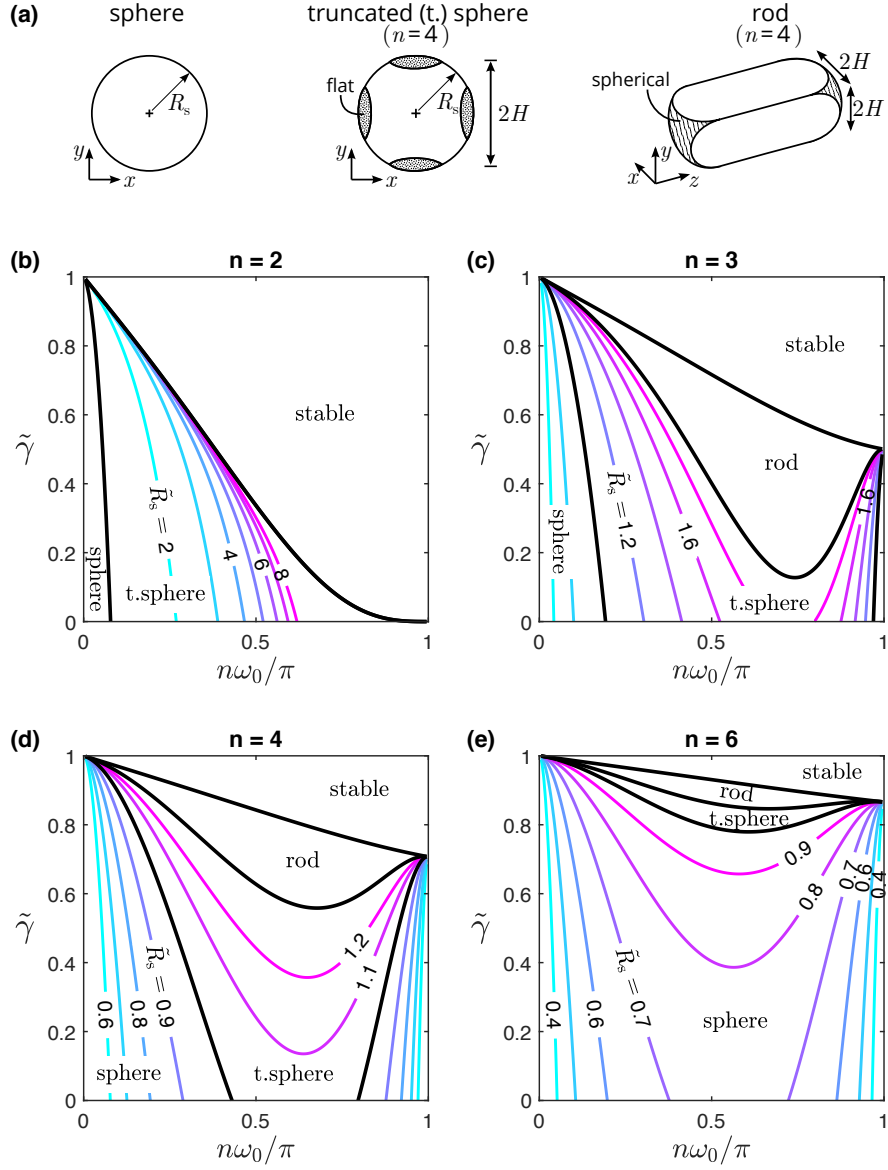
43

Figure 7: **(a)** The discrete particles emerging from pinch-off take the final form of spheres, truncated spheres (t. spheres), and rods. **(b)** to **(e)** Contours of the final, pinched-off radius of particle $\tilde{R}_{\mathrm{s}} = R_{\mathrm{s}}/H$ as a function of the surface energy ratio $\tilde{\gamma}$ and the initial contact angle ω_0 for a cylinder constrained by **(b)** $n = 2$, **(c)** $n = 3$, **(d)** $n = 4$, and **(e)** $n = 6$ necks. The topologies of the final particles are are marked on the maps.
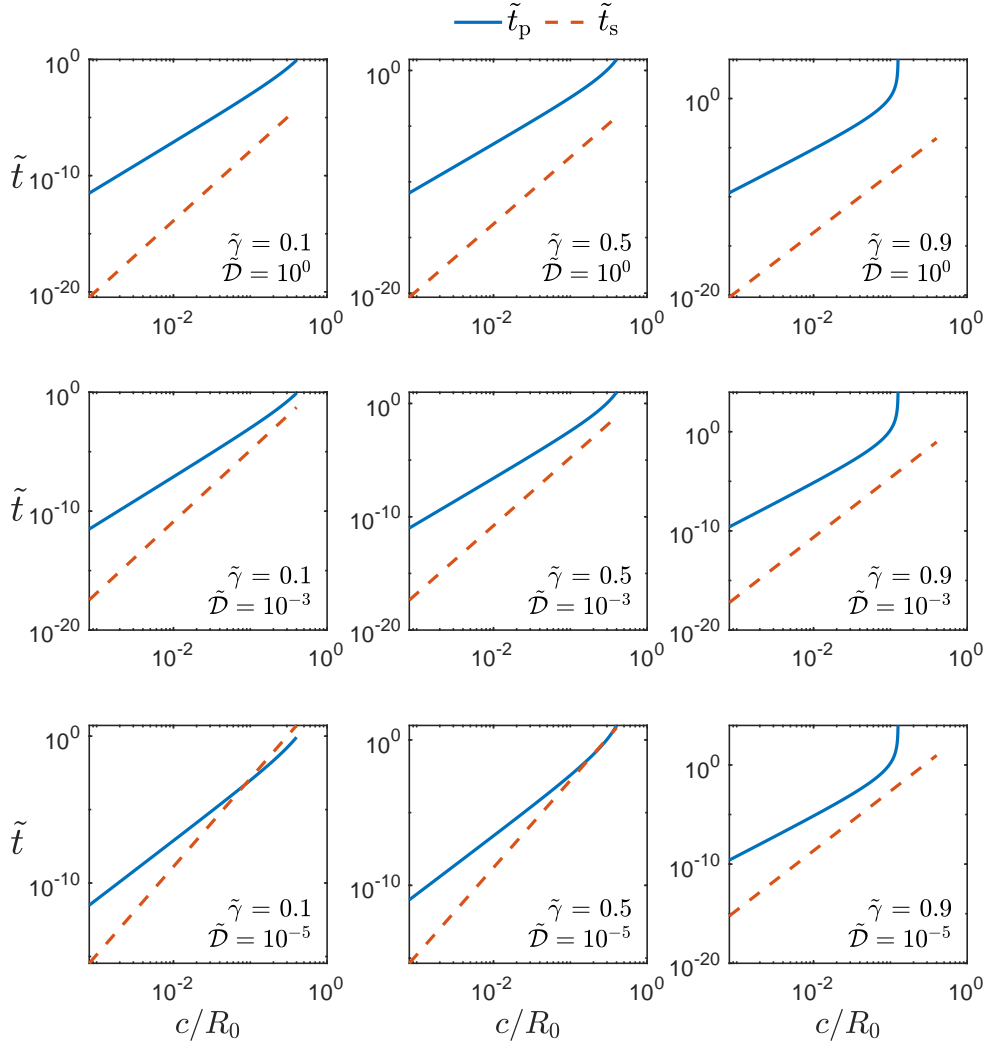
Figure 8: Pinch-off time $\tilde{t}_{\mathrm{p}} = \mathcal{D}_{\mathrm{s}}\gamma_{\mathrm{s}}t_{\mathrm{p}}/R_0^4$ of cylinders of contact width c/R_0 compared to the time $\tilde{t}_{\mathrm{s}} = \mathcal{D}_{\mathrm{s}}\gamma_{\mathrm{s}}t_{\mathrm{s}}/R_0^4$ to sinter a row of cylinders to establish the same value of c/R_0. Predictions are shown for selected combinations of relative diffusivity $\tilde{D} = \mathcal{D}_{\mathrm{c}}/\mathcal{D}_{\mathrm{s}}$ and relative surface energy $\tilde{\gamma} = \gamma_{\mathrm{c}}/\gamma_{\mathrm{s}}$.
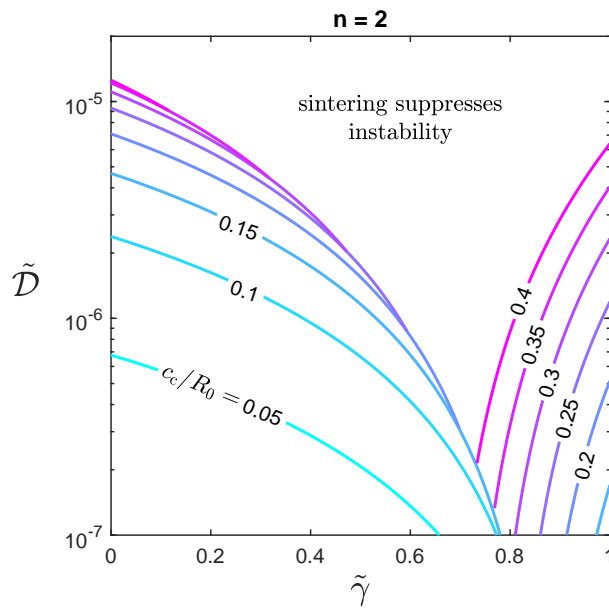
Figure 9: Contours of critical contact width c_c as a function of relative diffusivity $\tilde{D} = \mathcal{D}_c/\mathcal{D}_s$ and relative surface energy $\tilde{\gamma} = \gamma_c/\gamma_s$. For $c > c_c$, the pinch-off time t_p is shorter than the sintering time t_s. A region exists in the map where sintering is always faster than pinch-off, regardless of the contact width c, and consequently sintering suppresses the instability.

Appendix A. Stage I sintering of an array of circular cylinders

Our analysis of stage I sintering of an array of circular cylinders parallels that of Parhami et al. [51] who analyzed sintering of spheres. Consider an array of circular cylinders of initial radius R_0 with a center-to-center spacing of initial value $2H = 2R_0$ at time $t = 0$, as depicted in Fig. A.1. In stage I sintering, the cylinders maintain a constant radius R_0, the cylinder centers approach each other and a neck of width $2c$ grows. The driving force is the reduction in overall free energy associated with surface and interfacial energies. Assume a surface energy per unit area γ_s of the free surface of the cylinders and an interfacial energy per unit area γ_c of the contact zone. We proceed to obtain $c(t)$.

The initial cross-section of the cylinders in a unit cell at $t = 0$ is $A_z^0 = \pi R_0^2$, and after a time $t > 0$, it evolves to

$$A_z = \pi R_0^2 - \frac{4}{3}\frac{c^3}{R_0} + 4hc. \tag{A.1}$$

Conservation of mass requires $A_z = A_z^0$, and consequently

$$h = \frac{1}{3}\frac{c^2}{R_0} \tag{A.2}$$

and

$$H = R_0 - \frac{c^2}{6R_0}. \tag{A.3}$$

We use the same variational principle as defined in (30) with the definition of ΔG given in (18) in order to obtain $\dot{c}$. Assume that the dissipation in the

47

₇₇₂ grain boundary in stage I sintering dominates that over the free surface.

₇₇₃ Consequently, the dissipation potential reads

$$\Psi = \int_{A_c} \frac{j_c^2}{2\mathcal{D}_c} \, \mathrm{d}A_c, \tag{A.4}$$

₇₇₄ where we consider unit depth along the axis of the cylinder.

₇₇₅   Now obtain expressions for the surface and interface areas per unit depth.

₇₇₆ For the surface area, we have

$$A_s = 2\pi R_0 - 4c + \mathcal{O}(c^2), \tag{A.5}$$

₇₇₇ and $A_s^0 = 2\pi R_0$ for the initial surface area. For the contact area, we have

₇₇₈ $A_c = 2c$, and $A_c^0 = 0$. Upon inserting these areas into (18), we obtain

$$\Delta G = 2(\gamma_c - 2\gamma_s)c. \tag{A.6}$$

₇₇₉   Consider the kinematics of the diffusive flux. Conservation of mass re-

₇₈₀ quires that the divergence of the flux in the grain boundary and the velocity

₇₈₁ of matter into the grain boundary v_c sum to zero,

$$\boldsymbol{\nabla}_s \cdot \boldsymbol{j}_c + v_c = 0, \tag{A.7}$$

₇₈₂ where $\boldsymbol{\nabla}_s$ is the surface divergence operator. This relation simplifies to

₇₈₃ $\partial j_c / \partial x + v_c = 0$ for the in-plane problem. The velocity v_c is related directly

48

to the rate of change in height $2\dot{H}$ by $v_n = 2\dot{H}$, where

$$\dot{H} = -\frac{c\dot{c}}{3R_0}, \tag{A.8}$$

via (A.2) and (A.3). Consequently, the diffusive flux is

$$j_{\mathrm{c}} = \frac{2c\dot{c}x}{3R_0} \tag{A.9}$$

and (A.4) reduces to

$$\Psi = \frac{4c^5\dot{c}^2}{27\mathcal{D}_{\mathrm{c}}R_0^2}. \tag{A.10}$$

It remains to substitute (A.6) and (A.10) into (30), and to integrate with respect to time t to obtain

$$c^6 = \frac{81}{2}\mathcal{D}_{\mathrm{c}}R_0^2(2\gamma_{\mathrm{s}} - \gamma_{\mathrm{c}})t, \tag{A.11}$$

which is the same result as that obtained by [51] for an array of spheres, except for a small difference in pre-factor.
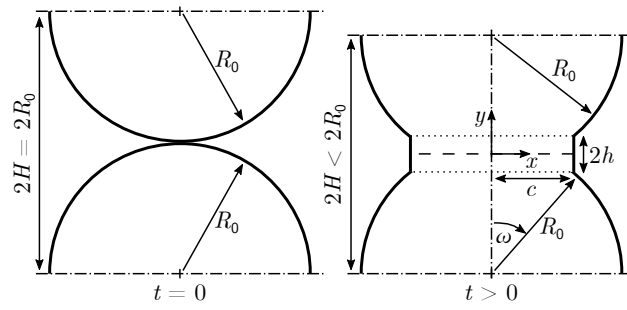
49

Figure A.1: Geometry of an array of circular cylinders undergoing stage I sintering.

Supplemetary Information to:
Stabilization of ultrathin nanowires
by self-assembly into bundles

Simon Bettscheider[a,c], Norman A. Fleck[b,*], Tobias Kraus[a,c,*]

*[a]INM – Leibniz Institute for New Materials, Campus
D2.2, Saarbrücken, 66123, Germany*
*[b]Cambridge University Engineering Department, Trumpington Street, Cambridge, CB2
1PZ, UK*
*[c]Colloid and Interface Chemistry, Saarland University, Campus
D2.2, Saarbrücken, 66123, Germany*

1. Chemicals

All chemicals used are listed in Tab. S1. Oleylamine was filtered prior to use (Millex filter, 0.45 µm, hydrophobic PTFE). All other chemicals were used as received.

Chemical	Purity	Manufacturer
Oleylamine	80-90 % C18	Acros Organics, PA, US
Hydrogen tetrachloroaurate trihydrate ($HAuCl_4 \cdot nH_2O$ with $n \approx 3$)	Au content $\geq 49\,\%$	Acros Organics, PA, US
Triisopropylsilane	$\geq 98\,\%$	abcr, Germany
n-hexane	$\geq 99\,\%$	abcr, Germany
Absolute ethanol	$\geq 99.8\,\%$	Fisher Scientific, PA, US
Cyclooctane	$\geq 99\,\%$	Alfa Aesar, MA, US

Table S1: Chemicals and manufacturers.

*Authors to whom correspondence should be addressed.
  Email addresses: `simon.bettscheider@leibniz-inm.de` (Simon Bettscheider), `naf1@eng.cam.ac.uk` (Norman A. Fleck), `tobias.kraus@leibniz-inm.de` (Tobias Kraus)

2. Scattering model

This section follows the work of Förster et al. [1], Sundblom et al. [2], Manet et al. [3], and Loubat et al. [4]. The total scattered intensity is the sum of the scattering contribution from spheres I_s, freely dispersed cylinders I_c, and bundled cylinders I_b. Consider each in turn.

2.1. Spheres

The intensity I_s scattered by a number n_s spheres is given by

$$I_s(q) = n_s(\rho_s - \rho_0)^2 P_s(q), \tag{1}$$

where ρ_s is the scattering length density of the sphere and ρ_0 that of the solvent. The term $P_s(q) = \langle F_s(q)^2 \rangle$ is the averaged form factor of the spheres, obtained by convoluting the form factor F_s of the spheres with a Schulz-Zimm distribution. The form factor $F_s(q)$ of the spheres is given by

$$F_s(q) = \left(\frac{4}{3}\pi R_s^2\right) \frac{3(\sin(qR_s) - qR_s \cos(qR_s))}{(qR_s)^3}. \tag{2}$$

The number of spheres n_s is related to the volume fraction of spheres ϕ_s via $n_s = \phi_s/\langle V_s \rangle$, where $\langle V_s \rangle$ is the average volume of a sphere. The intensity of the spheres can then be written as

$$I_s(q) = \phi_s(\rho_s - \rho_0)^2 \frac{\langle F_s^2(q) \rangle}{\langle V_s \rangle} \tag{3}$$

2.2. Freely dispersed nanowires

Freely dispersed nanowires were modeled as cylinders of radius R_c and length L with a scattered intensity of

$$I_c(q) = n_c(\rho_c - \rho_0)^2 P_c(q), \tag{4}$$

where n_c is the number of cylinders, ρ_c the scattering length density of the cylinder material, and $P_c(q)$ the averaged form factor of the cylinder. The averaged form factor of the cylinder $P_c(q)$ depends on the form factors of an infinitesimally thin cylinder $F_{\text{thin}}(q)$ and a disk's cross-section $F_{cs}(q)$ as $P_c(q) = F_{\text{thin}}(q)\langle F_{cs}^2(q)\rangle$. The form factor of the cross-section $F_{cs}(q)$ is given by

$$F_{cs}(q) = \pi R_c^2 \frac{2J_1(qR_c)}{qR_c}, \tag{5}$$

where J_1 is the Bessel function of the first kind. The form factor of the infinitesimally thin cylinder is given by

$$F_{\text{thin}}(q) = L^2 \left(\frac{2}{qL} \int_0^{qL} \frac{\sin(x)}{x} \mathrm{d}x - \left(\frac{2\sin(qL/2)}{qL} \right)^2 \right) \tag{6}$$

In the case of $q \gg 1/L$, which is valid in our scattering experiments, the integral may be approximated by $\int_0^{qL} \frac{\sin(x)}{x} \mathrm{d}x \approx \frac{\pi}{2}$ so that the form factor $F_{\text{thin}}(q)$ simplifies to

$$F_{\text{thin}}(q) = L^2 \left(\frac{\pi}{qL} - \left(\frac{2\sin(qL/2)}{qL} \right)^2 \right) \tag{7}$$

In analogy to the spheres, the number of cylinders n_{c} is related to the volume fraction of freely dispersed cylinders ϕ_{c} via $n_{\text{c}} = \phi_{\text{c}}/\langle V_{\text{c}} \rangle$, where $\langle V_{\text{c}} \rangle$ is the average volume of a cylinder. The scattered intensity of the freely dispersed cylinders can hence be written as

$$I_{\text{c}}(q) = \phi_{\text{c}}(\rho_{\text{c}} - \rho_0)^2 \frac{F_{\text{thin}}(q) \langle F_{\text{cs}}^2(q) \rangle}{\langle V_{\text{c}} \rangle}. \tag{8}$$

2.3. Bundled nanowires

Bundled nanowires were modeled as the average over a 2D close-packed (hexagonal) lattice of cylinders. The scattered intensity is the one of cylinders given in (8), multiplied by lattice factor of a disordered lattice $Z(q)$ as given by

$$I_{\text{d}}(q) = \phi_{\text{d}}(\rho_{\text{c}} - \rho_0)^2 \frac{F_{\text{thin}}(q) \langle F_{\text{cs}}^2(q) \rangle}{\langle V_{\text{c}} \rangle} Z(q). \tag{9}$$

The lattice factor of the disordered lattice is given by

$$Z(q) = \beta(q)G(q)Z_0(q) + (1 - \beta(q)G(q)), \tag{10}$$

where $Z_0(q)$ is the lattice factor of an ideal lattice, $\beta(q)$ accounts for disorder in the lattice due to polydispersity of the cylinder radius, and $G(q)$ if the Debye-Waller factor accounting for disorder caused by thermal fluctuations. The lattice factor of an ideal lattice of unit cell area A_{unit}, peak multiplicites m_{hk}, and peak positions q_{hk} is given by

$$Z_0(q) = \frac{1}{A_{\text{unit}}} \frac{2\pi}{q} \sum_{hk} m_{hk} L_{hk}(q, q_{hk}, \sigma). \tag{11}$$

3

Here, $L_{hk}(q, q_{hk}, \sigma)$ is the normalized Lorentz function with a peak width of 2σ. The term accounting for lattice disorder due to polydispersity in the cylinder radius $\beta(q)$ is given by

$$\beta(q) = \frac{\langle F_{\text{cs}} \rangle^2}{\langle F_{\text{cs}}^2 \rangle} \tag{12}$$

and the Debye-Waller factor $G(q)$ is given by

$$G(q) = \exp\left(-\sigma_{\text{DW}}^2 a^2 q^2\right), \tag{13}$$

where σ_{DW} is the relative mean-square displacement for the positional disorder, and a is the distance between the nearest neighbors, which is identical to the lattice constant in the close-packed, hexagonal lattice.

3. Additional figures

The relative density (also called packing density) $\bar{\rho}$ can be calculated for $n \geq 3$ and is given by

$$\bar{\rho} = \frac{\cot\left(\pi/n\right)}{\cos^2 \omega_0} \left(\frac{\pi}{n} - \frac{1}{2}\left(2\omega_0 - \sin\left(2\omega_0\right)\right)\right). \tag{14}$$

Values of the relative density $\bar{\rho}$ are given for example configurations in S2, and $\bar{\rho}$ is plotted as a function of n and ω_0 in S3a.
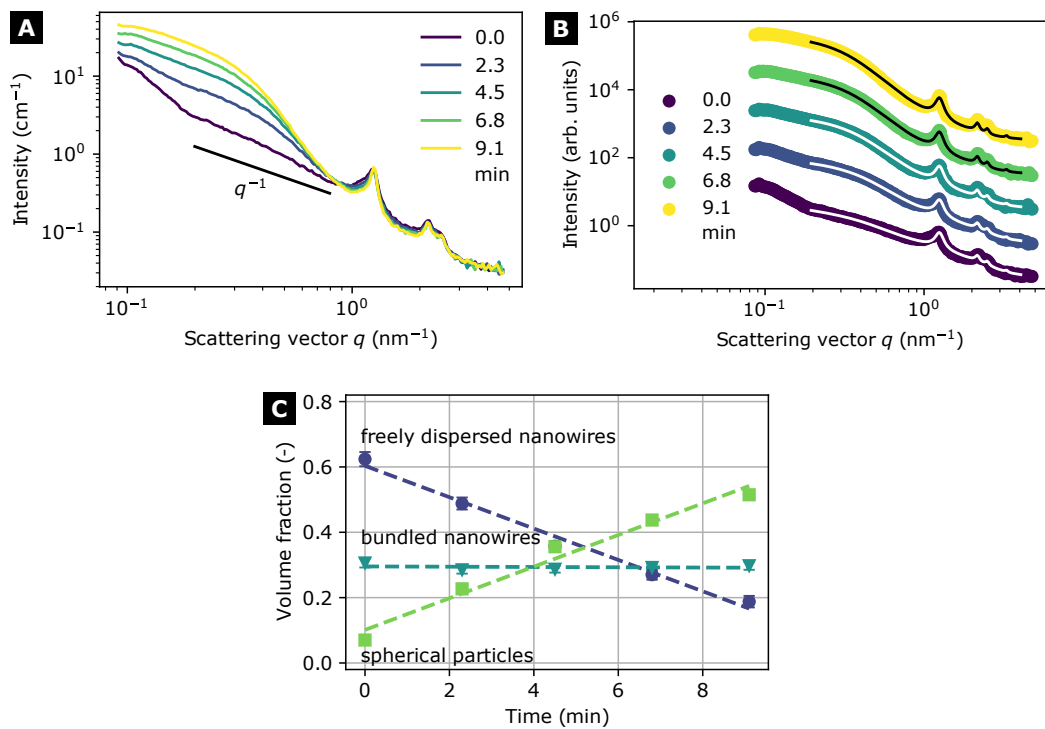
Figure S1: **(a)** Evolution of small-angle X-ray scattering from fragmenting AuNWs at 70 °C. At small q-values, the scattering signal bulges upwards, indicating that nanowires have broken-up into spheroidal particles. **(b)** Scattering models fitted to the scattering from **(a)** at selected times. Dots show experimental data points and solid lines the fits; the scattering curves are shifted vertically for better visualisation. **(c)** Volume fractions of gold in freely dispersed nanowires, bundled nanowires, and spherical particles. Error bars denote the standard error of the fits. The dashed line are linear fits.
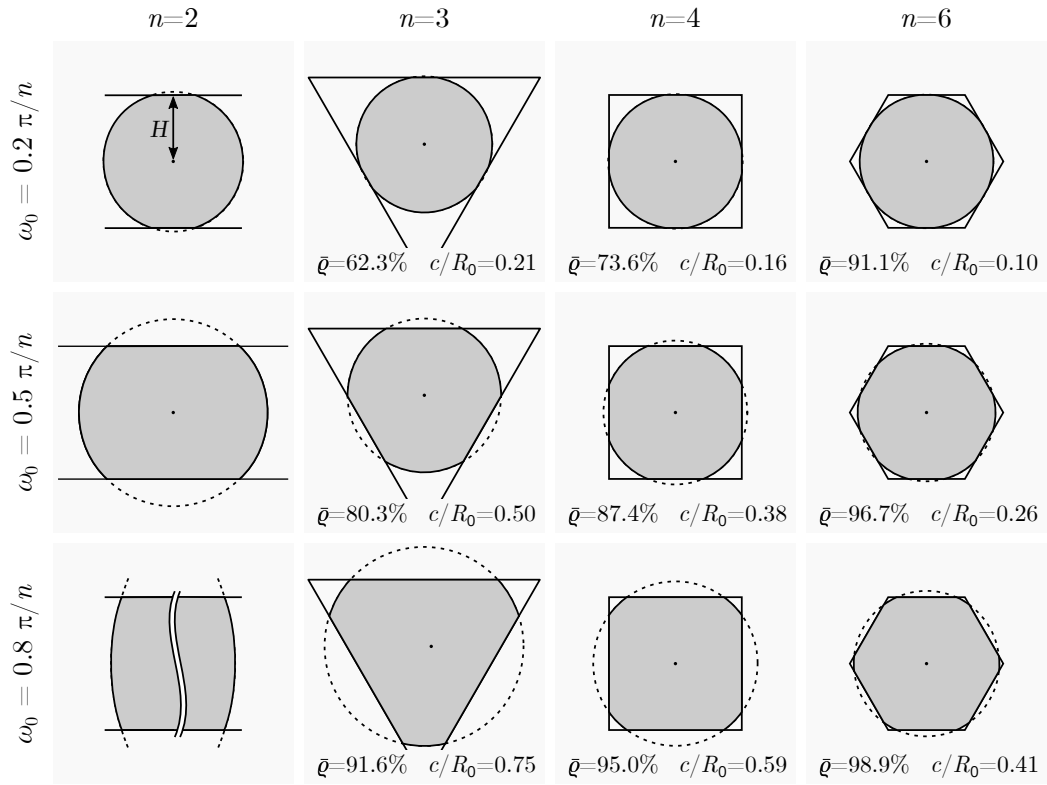
Figure S2: Example configurations a cylinder truncated by n facets at three different contact angles ω_0. The height H, which is the distance between the cylinders centre and the truncating surfaces, is constant among all shown configurations. For $n \geq 3$, the relative density (also called packing density) $\bar{\rho}$ and the contact width c/R_0 are shown.
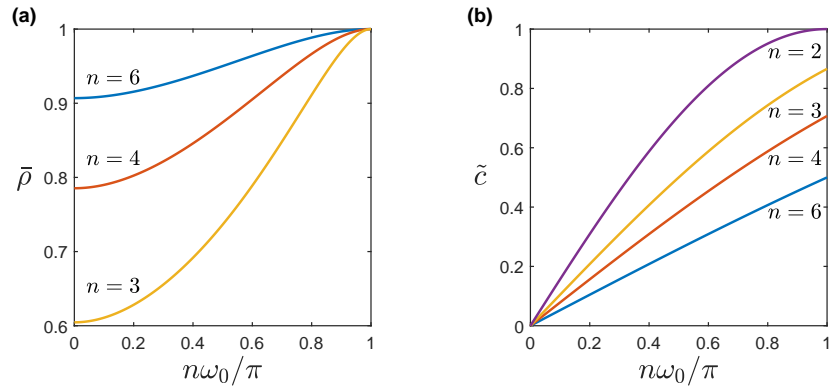
Figure S3: **(a)** Packing density $\bar{\rho}$ as a function of the contact angle ω_0 for the tesselated arrangements of truncated cylinders as shown in Fig. S2. **(b)** The contact width $\tilde{c} = c/R_0$ as a function of contact angle ω_0.

References

[1] S. Förster, A. Timmann, M. Konrad, C. Schellbach, A. Meyer, S. S. Funari, P. Mulvaney, R. Knott, Scattering Curves of Ordered Mesoscopic Materials, Journal of Physical Chemistry B 109 (2005) 1347–1360. URL: `http://pubs.acs.org/doi/abs/10.1021/jp0467494`. doi:`10.1021/jp0467494`.

[2] A. Sundblom, C. L. P. Oliveira, A. E. C. Palmqvist, J. S. Pedersen, Modeling in Situ Small-Angle X-ray Scattering Measurements Following the Formation of Mesostructured Silica, The Journal of Physical Chemistry C 113 (2009) 7706–7713. URL: `https://pubs.acs.org/doi/10.1021/jp809798c`. doi:`10.1021/jp809798c`.

[3] S. Manet, J. Schmitt, M. Impéror-Clerc, V. Zholobenko, D. Durand, C. L. P. Oliveira, J. S. Pedersen, C. Gervais, N. Baccile, F. Babonneau, I. Grillo, F. Meneau, C. Rochas, Kinetics of the Formation of 2D-Hexagonal Silica Nanostructured Materials by Nonionic Block Copolymer Templating in Solution, The Journal of Physical Chemistry B 115 (2011) 11330–11344. URL: `https://pubs.acs.org/doi/10.1021/jp200213k`. doi:`10.1021/jp200213k`.

[4] A. Loubat, M. Impéror-Clerc, B. Pansu, F. Meneau, B. Raquet, G. Viau, L.-M. Lacroix, Growth and Self-Assembly of Ultrathin Au Nanowires into Expanded Hexagonal Superlattice Studied by in Situ SAXS, Langmuir 30 (2014) 4005–4012. URL: `https://pubs.acs.org/doi/10.1021/la500549z`. doi:`10.1021/la500549z`.